Journal of Applied Physics ARTICLE scitation.org/journal/jap

Sensitive radiofrequency readout of quantum dots using an ultra-low-noise SQUID amplifier

Cite as: J. Appl. Phys. **127**, 244503 (2020); doi: 10.1063/5.0005886
Submitted: 25 February 2020 · Accepted: 14 June 2020 ·
Published Online: 29 June 2020

View Online Export Citation CrossMark

F. J. Schupp,[1] F. Vigneau,[1] Y. Wen,[1] A. Mavalankar,[1] J. Griffiths,[2] G. A. C. Jones,[2] I. Farrer,[2,3] D. A. Ritchie,[2] C. G. Smith,[2] L. C. Camenzind,[4] L. Yu,[4] D. M. Zumbühl,[4] G. A. D. Briggs,[1] N. Ares,[1] and E. A. Laird[1,5,a)]

AFFILIATIONS

[1]Department of Materials, University of Oxford, 16 Parks Road, Oxford OX1 3PH, United Kingdom
[2]Cavendish Laboratory, J.J. Thomson Avenue, Cambridge CB3 0HE, United Kingdom
[3]Department of Electronic and Electrical Engineering, University of Sheffield, Sheffield S1 3JD, United Kingdom
[4]Department of Physics, University of Basel, 4056 Basel, Switzerland
[5]Department of Physics, University of Lancaster, Lancaster LA1 4YB, United Kingdom

[a)]**Author to whom correspondence should be addressed:** e.a.laird@lancaster.ac.uk

ABSTRACT

Fault-tolerant spin-based quantum computers will require fast and accurate qubit read out. This can be achieved using radiofrequency reflectometry given sufficient sensitivity to the change in quantum capacitance associated with the qubit states. Here, we demonstrate a 23-fold improvement in capacitance sensitivity by supplementing a cryogenic semiconductor amplifier with a SQUID preamplifier. The SQUID amplifier operates at a frequency near 200 MHz and achieves a noise temperature below 600 mK when integrated into a reflectometry circuit, which is within a factor 120 of the quantum limit. It enables a record sensitivity to capacitance of 0.07 aF/$\sqrt{\text{Hz}}$. The setup is used to acquire charge stability diagrams of a gate-defined double quantum dot in a short time with a signal-to-noise ration of about 38 in 1 μs of integration time.

I. INTRODUCTION

Electron spins in semiconductors are among the most advanced qubit implementations and are a potential basis of scalable quantum computers fabricated using industrial processes.[1–3] A useful computer must correct the errors that inevitably arise during a calculation, which requires high single-shot qubit readout fidelity.[4] The full surface code for error detection requires approximately half the physical qubits to be read out in every clock cycle of the computer.[5] Until recently, a single-shot readout in spin qubit devices could only be achieved via spin-to-charge conversion and detected by a nearby single-electron transistor (SET) or quantum point contact (QPC) charge sensor.[6–9] However, the hardware is simpler and smaller if it uses dispersive readout, which exploits the difference in electrical polarizability between the singlet and triplet spin states in a double quantum dot.[10–13] The resulting capacitance difference between the two qubit states can be monitored via a radiofrequency (RF) resonator bonded to one of the quantum dot electrodes. Similar dispersive shifts also occur at charge transitions in the quantum dots such that the reflected signal assists with tuning the desired electron occupation.[14–16] Dispersive readout has the advantage that it does not require a separate charge sensor, but often the capacitance sensitivity is insufficient for single-shot qubit readout even in systems with a long spin decay time.[17–23] Recently, there have been demonstrations of dispersive single-shot readout in double quantum dot based systems,[24–28] but higher sensitivities are still desirable for improved readout fidelity.

High sensitivity also makes it possible to rapidly measure charge stability diagrams and, therefore, speeds up quantum dot tuning. For example, fast measurement has enabled video-mode tuning using an RF setup attached to one of the electrodes of a double quantum dot.[29] Auto-tuning techniques,[30–32] which are often limited by measurement time, also benefit from the increased measurement speed.

High-fidelity readout, whether dispersive or using a charge sensor, relies on low-noise amplifiers to attain good capacitance

sensitivity. Radiofrequency experiments until now have used semiconductor amplifiers cooled to ∼4 K. Even lower noise can be achieved using amplifiers based on superconducting quantum interference devices (SQUIDs). At microwave frequencies, Josephson parametric amplifiers (JPAs) and traveling wave parametric amplifiers approach the quantum limit of sensitivity.[33–35] Such amplifiers allow rapid measurements of charge parity in a double quantum dot.[29,37] However, the JPAs previously used for quantum dot readout have a linear amplification range limited to an input power of −130 dBm,[29,36] they require a circulator inside the cryostat and a dedicated pump oscillator, and they are not commercially available. Most JPAs are optimized for a microwave frequency range well above 1 GHz, although operation as low as 650 MHz has been demonstrated.[36] However, a lower frequency is desirable because the charge dipole in a singlet–triplet qubit only responds adiabatically to changes in the electric field if the interdot tunnel rate is much larger than the readout frequency. If, on the other hand, the readout frequency approaches the inter-dot tunnel rate, the quantum capacitance is suppressed and readout times increase.[38] Increasing the tunnel rate leads to inelastic spin relaxation,[39] and it is, therefore, usually limited to no more than a few GHz.[10,40]

Here, we demonstrate a radiofrequency reflectometry circuit, operating at 196 MHz, that employs a SQUID as the primary amplifier.[41] We find an amplifier noise temperature below 600 mK. This enables the reflectometry circuit to detect a capacitance signal with a sensitivity better than 0.1 aF/$\sqrt{\text{Hz}}$. Attaching the reflectometry circuit to the ohmic contact of a GaAs double quantum dot, we acquire a Coulomb stability diagram with a resolution of 100 × 100 points within 20 ms. The measurement time to distinguish the two states of a singlet–triplet qubit using gate-based capacitance sensing is estimated to be well below 1 μs even at low excitation power. This time should be short enough for a single-shot readout.

This paper is organized as follows. Section II describes the measurement setup and its principle of operation. In Sec. III, we characterize the amplifier and show how to optimize its noise and gain by adjusting the control bias settings. In Sec. IV, we tune the resonant tank circuit used in the reflectometry setup and measure the capacitance sensitivity using a variable capacitor (varactor). The setup used in Secs. III and IV contains a single quantum dot device that serves as a realistic load on the tank circuit. In Sec. V, this device is replaced by a double quantum dot, and the reflectometry circuit is used to measure the stability diagram and to estimate the minimum acquisition time. Section VI summarizes and evaluates the potential for the qubit readout. Further technical details and measurements of the single quantum dot appear in the supplementary material.

II. MEASUREMENT SETUP

Figure 1 shows the reflectometry circuit used in the experiment. It is designed to sensitively measure two kinds of signal: changing capacitance in a varactor and changing charge configuration in a laterally defined quantum dot. We have previously characterized these sensitivities using the same setup without the SQUID amplifier.[18] Quantum dots of the kind used in this experiment are defined in a GaAs/AlGaAs two-dimensional electron gas (2DEG) by applying depletion voltages to top gates. Here, we use the device

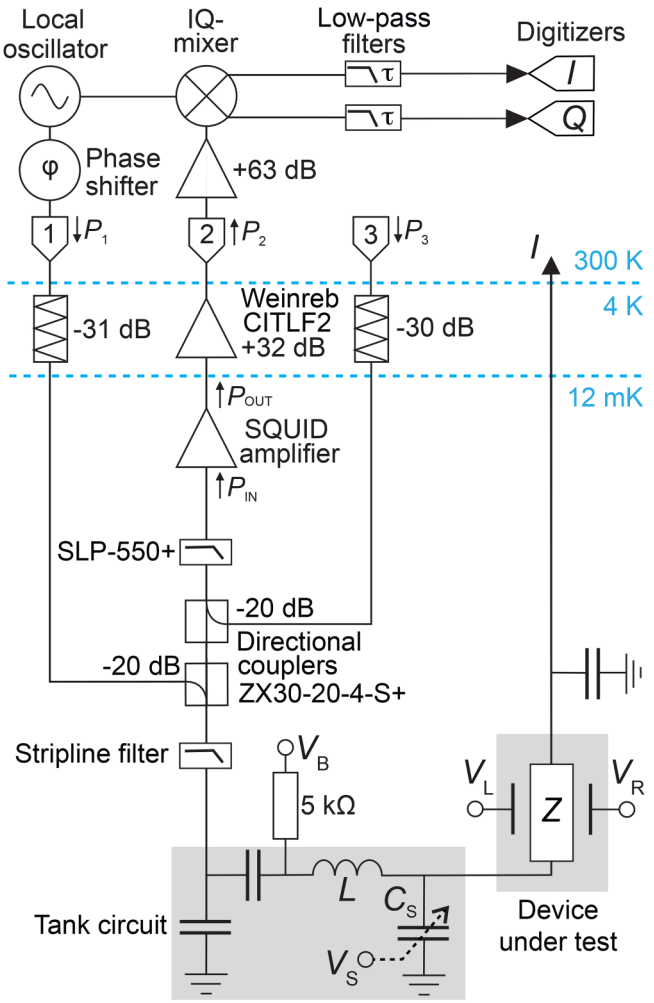

FIG. 1. Experimental setup. Measurements were performed in a dilution refrigerator at its base temperature of 12 mK. A resonant tank circuit is defined by a surface mount inductor $L = 223$ nH and capacitors, including a varactor tuned by voltage V_S. To excite this circuit, an RF carrier tone is generated by a local oscillator, phase shifted, injected into port 1 of the refrigerator with power P_1, and launched toward the tank circuit via cryogenic attenuators and a directional coupler. The reflected signal is amplified first by the SQUID and then by a semiconductor postamplifier, before it is fed via port 2 of the refrigerator to a homodyne mixing circuit to demodulate the signal into two voltages V_I and V_Q that represent the I and Q quadratures. Alternatively, the output from port 2 is measured using a spectrum analyzer or network analyzer (not shown). A second injection path via port 3 is used to calibrate the amplifier chain. The tank circuit is loaded by a device under test with impedance Z. For the experiments in Secs. III and IV, Z is a quantum dot fully pinched off using gate voltages V_L and V_R. For the experiments in Sec. V, Z is a double quantum dot.

shown in Fig. 2 in which a quantum dot is defined by gate voltages V_L and V_R and measured via source and drain contacts to the 2DEG. For the experiments of Secs. III and IV, this device was incorporated into the measurement circuit; however, in order to

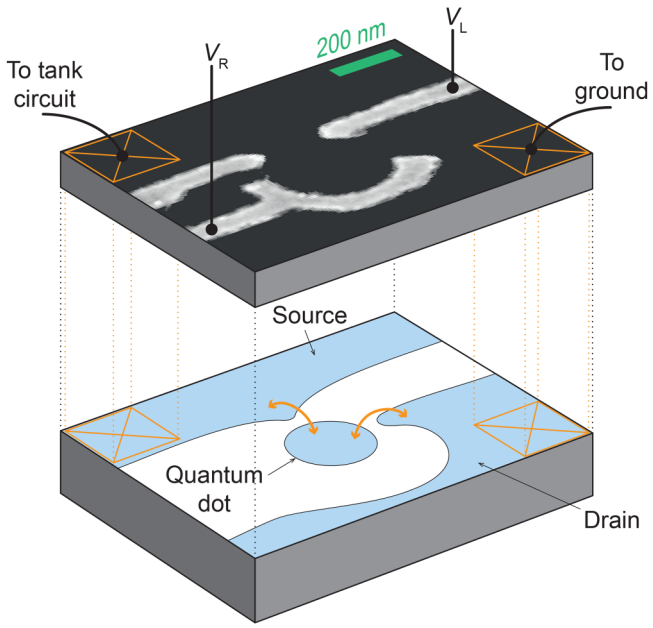

FIG. 2. Exploded plan of a GaAs quantum dot of the design used in this experiment.[18,42] The device consists of a GaAs/AlGaAs heterostructure wafer containing a two-dimensional electron gas 90 nm beneath the surface. On the surface of the wafer, Ti/Au gates are fabricated, as shown in the scanning electron microscope image (top). Negative voltages applied to these gates selectively deplete the electron gas, defining source and drain regions and a quantum dot. The source and drain are connected to the tank circuit and to ground by ohmic contacts, schematically indicated by squares. Electron tunneling between source, dot, and drain contributes to the conductance and capacitance between the tank circuit and ground. For the experiments in Secs. III and IV, the dot is fully pinched off (i.e., electron tunneling is nearly suppressed) using very negative gate voltages V_L and V_R. The double quantum dot of Sec. V operates on the same principle.

characterize the SQUID independently of the quantum dot, the dot was configured for very small conductance by applying large negative gate voltages and thereby also depleted of electrons.

The quantum dot device is wire-bonded to the RF circuit that was assembled from chip components on a printed circuit board. The RF circuit includes a fixed inductor L, a varactor of capacitance C_S tuned by a voltage V_S, and a terminal through which a DC source-drain bias voltage V_B is applied to the quantum dot device (Fig. 1). These components form a resonant tank circuit with a total impedance that depends on the quantum dot impedance, the varactor tuning voltage, and the RF frequency. The circuit board is mounted on a 12 mK dilution refrigerator wired for reflectometry measurements. An RF input line (port 1) injects power into the tank circuit via a directional coupler. The reflected signal is passed to a SQUID amplifier at base temperature, boosted by a semiconductor postamplifier at 4 K, and then measured at port 2. Once this amplifier chain is configured appropriately, its noise is dominated by the SQUID amplifier, which, therefore, sets the measurement sensitivity.[18] A second RF input line (port 3), coupled via an oppositely oriented directional coupler, allows calibrated signals to be injected directly into the RF measurement line to characterize the amplifier chain independently of the resonant circuit. Both input lines contain attenuators to suppress thermal noise.

The SQUID amplifier is shown schematically in Fig. 3(a). It exploits the fact that the critical current of a DC SQUID depends on the instantaneous magnetic flux enclosed between the junctions. To operate the amplifier, an input signal V_{IN} is fed into a 20-turn superconducting coil, acting as an open-ended transmission line, through which it excites an oscillating magnetic field. The coil is fabricated over a Nb-based SQUID, separated by a 400 nm SiO_2 spacer layer, following the "washer" geometry shown in Fig. 7(b) of Ref. 41. The SQUID is biased with a current I_B set greater than the maximum critical current. The resulting junction voltage V_{OUT} depends on the instantaneous critical current, and its variation constitutes the amplifier's output signal.[41] To optimize the gain, a flux offset is applied by means of a flux bias current I_Φ applied to a nearby coil. The resonant frequency and quality factor of the input coil determine the optimum operating frequency and the bandwidth. The length of this input coil is chosen according to the desired operation frequency, since the gain peaks at a frequency that corresponds to approximately half a wavelength in the input coil.[41] The geometry was chosen to give an operating frequency near 200 MHz with a bandwidth around 60 MHz. Figure 3(b) shows a photograph of the amplifier with connectors. The picture also shows a shield, made of lead and Conetic QQ foil, into which the amplifier is inserted to suppress flux noise.

For frequency-domain experiments, the output at port 2 is measured directly using a spectrum analyzer or a network analyzer. For time-domain measurements, the signal is homodyne demodulated using a lock-in amplifier to yield in-phase and quadrature signals I and Q, each filtered with time constant τ as in the circuit of Fig. 1.

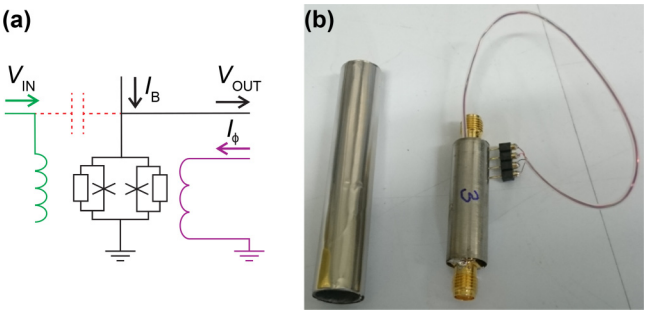

FIG. 3. (a) SQUID amplifier schematic, showing SQUID bias current I_B, flux bias current I_Φ, and input and output voltages V_{IN} and V_{OUT}. The dashed capacitance between V_{IN} and V_{OUT} represents a parasitic capacitance when referring to the setup used in Secs. III and IV. In the setup discussed in Sec. V, the dashed capacitor also represents an additional feedback capacitor, introduced to lower the input impedance of the amplifier. Each Josephson junction is shunted by a 30 Ω resistor. (b) Photograph of a packaged amplifier (right) and its shield (left). Coaxial SMA connectors at bottom and top are RF input and output; the DC wires leading to a header connector are used to supply I_Φ, I_B, a heating current, and DC ground. Although the heater was not used in our experiment, it could be used to remove trapped flux by heating the SQUID above the critical temperature.

III. CHARACTERIZING AND TUNING THE AMPLIFIER

We begin by characterizing the amplifier's gain and noise. To achieve optimized signal-to-noise performance, we follow a tuning procedure that adjusts the current bias across the SQUID, the flux offset and the input power. For the measurements in this section, the amplifier is driven by direct injection into port 3, and the output from port 2 is measured using a spectrum analyzer (see Fig. 1). The injected tone has a frequency $f_C = 196$ MHz, chosen for later compatibility with the tank circuit. For the measurements as a function of I_B and I_Φ, we set the power at port 3 to be $P_3 = -89$ dBm, corresponding to a power $P_{IN} = -139$ dBm at the SQUID input. The SQUID amplifier gain is determined by comparing the total transmission from port 3 to port 2 with the amplifier present, vs an identical measurement in which it is replaced by a short length of cable. The gain is

$$\frac{P_{OUT}}{P_{IN}} = \frac{|S_{32}|^2(\text{amplifier present})}{|S_{32}|^2(\text{amplifier absent})}, \tag{1}$$

where P_{OUT} is the power at the amplifier output. The noise power is then determined by injecting a signal tone with power P_{IN} into the SQUID amplifier input and measuring the output spectrum at port 2. The noise power referred to the amplifier input is then

$$P_N = P_{IN}\frac{P_2(\text{noise})}{P_2(\text{signal})}, \tag{2}$$

where P_2(signal) is the power of the amplified signal tone and P_2(noise) is the noise power, both measured at port 2. The system noise power can then be expressed as a noise temperature

$$T_N = \frac{P_N}{k_B \Delta f} - T, \tag{3}$$

where Δf is the resolution bandwidth of the spectrum analyzer and T is the noise temperature of the input signal into the SQUID amplifier. To accurately determine the power level P_{IN}, which depends on the transmission characteristics of the cables, we separately measured the attenuation of the injection path (see the supplementary material). To avoid underestimating the system noise temperature, we assume the lowest possible electron temperature given perfect thermalization, i.e., $T = 12$ mK. (In fact, our typical estimated electron temperature is $T \approx 25$ mK.[43]) This assumption and the possibility of reflections on the amplifier input make T_N an upper limit to the noise temperature of the SQUID amplifier.

Optimum operation, i.e., high amplifier gain and low noise, requires us to find suitable settings for both I_B and I_Φ. We follow a two-step process. First, we increase I_B until a change in P_{OUT} is detected, indicating that the critical current has been exceeded. Next, we optimize the flux offset Φ via I_Φ to find a steep point in the function $V_{OUT}(\Phi)$ so that the output voltage is most sensitive to the induced flux.

Figure 4 shows the performance of the amplifier as a function of the bias currents I_B [Figs. 4(a) and 4(c)] and I_Φ [Figs. 4(b) and 4(d)]. At low I_B, the SQUID is biased below its critical current and only a fraction of the input power is transmitted to the output by capacitive leakage. As I_B is increased above the critical current, a voltage develops and the gain increases abruptly. This occurs at $I_B \approx 10.7\,\mu$A in Fig. 4(a). At larger currents, the gain varies non-monotonically due to the self-inductance of the SQUID.[44] These variations can be compensated by adjusting I_Φ, and in fact, we find that a similar gain can be achieved for all chosen values of I_B larger than the critical current. Because the critical current depends on the flux, the chosen I_B should be larger than the critical current for all I_Φ.

We now measure the gain as a function of flux bias current I_Φ [Fig. 4(b)]. For this measurement, we choose $I_B = 13.1\,\mu$A [black marker in Figs. 4(a) and 4(c)]. At first sight, Fig. 4(a) implies that I_B is larger than optimal; the reason to choose this value is that on

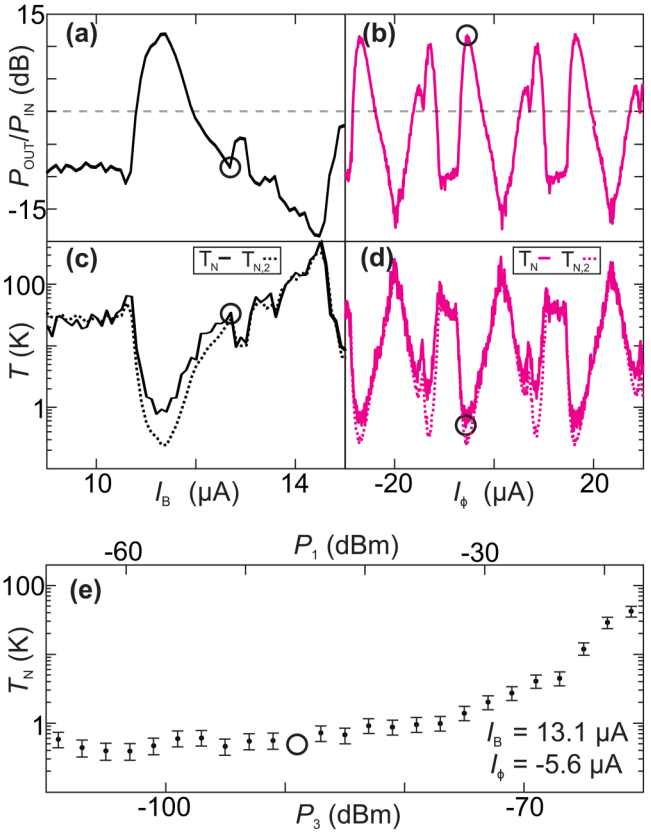

FIG. 4. (a)–(d) show the characterization of the SQUID amplifier as a function of the current bias I_B (black) and the flux coil bias I_Φ (purple) at frequency 196 MHz and power into port 3 $P_3 = -89$ dBm. (a) Gain as a function of bias with $I_\Phi = 0$. The gray dashed line marks 0 dB. (b) Gain as a function of flux bias current at $I_B = 13.1\,\mu$A. (c) Noise temperature T_N as a function of I_B determined for every point in (a). The dashed line is the postamplifier contribution $T_{N,2}$. (d) Noise temperatures T_N (line) and $T_{N,2}$ (dashed line) as a function of I_Φ. The black markers indicate the chosen settings ($I_B = 13.1\,\mu$A and $I_\Phi = -5.6\,\mu$A) in the rest of Secs. III and IV, giving gain ≈12 dB and $T_N \approx 480$ mK. (e) Noise temperature as a function of input power into port 3 P_3 (bottom axis). The top axis shows the estimated corresponding input power into port 1 P_1, assuming $|S_{21}| = -49.98$ dB from the best matching condition in Fig. 5. The black circle indicates the power used in (a)–(d).

a previous cooldown, the critical current was as high as 12.9 μA at $I_\Phi = 0$ (see the supplementary material). By choosing I_B above this value, we aim for it to be well above the critical current for all flux-offsets but not large enough to significantly heat the SQUID.

As shown in Fig. 4(b), the gain varies periodically with I_Φ, reflecting the periodic dependence of critical current on flux. For an ideal SQUID at high current bias, the gain would be a sinusoidal function of flux. In fact, this amplifier has a more complex periodic dependence, which indicates that self-heating, junction asymmetry, and/or parasitic impedances play important roles in determining the gain.[44] For example, junction asymmetry would unequally divide the bias current between the two arms of the SQUID, leading to a changing flux. To optimize the sensitivity, we choose $I_\Phi = -5.6\,\mu$A [black marker in Figs. 4(b) and 4(d)], leading to a gain of 11.7 $\pm$ 0.8 dB. The uncertainty of this value is accumulated over multiple measurements that are needed to determine the losses of the insertion path and the gain of the postamplifier.

Figures 4(c) and 4(d) show the system noise temperature T_N as a function of I_B and of I_Φ, respectively. In both traces, the same bias settings that maximize the gain also lead to low noise. To distinguish the noise of the SQUID from the noise of the postamplifier, we plot as a dashed curve on the same axes the postamplifier's contribution to the system noise temperature

$$T_{N,2} = T_P \frac{P_{IN}}{P_{OUT}}, \tag{4}$$

where $T_P = 3.7$ K is the input noise temperature of the postamplifier. This is the lowest noise temperature (referred to the SQUID input) that the system could achieve if the SQUID were a noiseless amplifier. Over most of the range, this contribution is approximately equal to the entire system noise ($T_N \approx T_{N,2}$), meaning that the intrinsic noise of the SQUID is indeed undetectable. However, the optimal bias settings, with the highest gain, the lowest noise, and, therefore, the best signal-to-noise ratio, lead to $T_N > T_{N,2}$, showing that for these settings the system noise is dominated by the SQUID contribution. Previous experiments have found this contribution to arise from hot electrons generated by ohmic dissipation.[41,45,46] There may also be a contribution from thermal radiation leaking into the SQUID. The lowest noise temperature observed is $T_N = 500 \pm 100$ mK, obtained with $I_\Phi = -5.6\,\mu$A [black marker in Fig. 4(d)]. This is within a factor 120 of the quantum limit $hf_C/2k_B = 5$ mK.[47]

To study the amplifier dynamic range, Fig. 4(e) shows the noise temperature as a function of input power P_3. The top axis shows an estimate of the corresponding power P_1 into port 1 that leads to the same power at the SQUID input when it is used for a reflectometry experiment (assuming that the matching circuit is optimized, as discussed below in Sec. IV A and Fig. 5). The noise increases at high input power, with the threshold being approximately $P_3 \approx -70$ dBm, which corresponds to an amplifier input power of approximately $P_{IN} \approx -120$ dBm. The input power corresponding to the onset of amplifier saturation can be roughly estimated from the SQUID parameters given by the manufacturer to be $P_{IN} \approx -100$ dBm (see the supplementary material). The lower dynamic range of the amplifier in our setup and the elevated noise temperature (compared to the state of the art in setups dedicated to optimized SQUID amplifier performance rather than sensitive RF readout) could be related to poor input impedance matching between the SQUID and the 50 Ω components in the circuit, to radiation from outside the refrigerator, or to incomplete thermalization.[41]

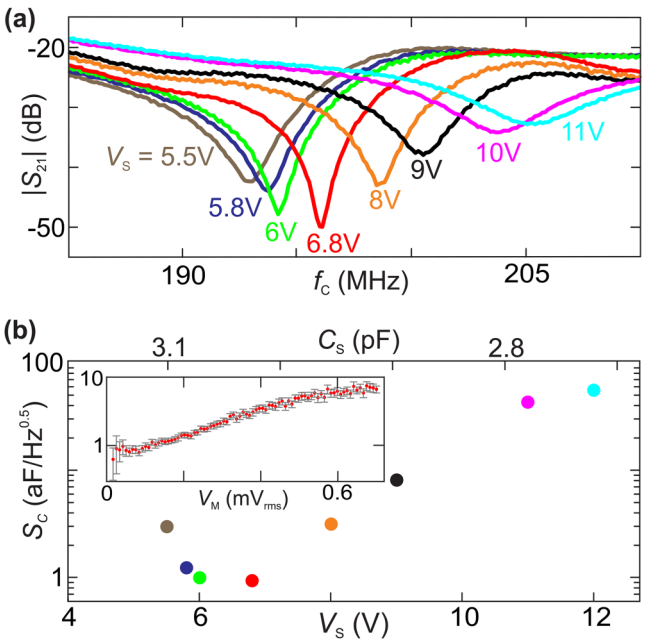

FIG. 5. (a) Transmission $|S_{21}|$ from port 1 to port 2 as a function of carrier frequency f_C at the varactor voltage settings indicated. (b) Capacitance sensitivity S_C as a function of varactor voltage V_S, measured with a modulation frequency $f_M = 3$ kHz, modulation amplitude $V_M = 99\,\mu V_{rms}$ (corresponding to a capacitance modulation of $\delta C = 6.7\,aF_{rms}$) and carrier power $P_1 = -60$ dBm. The carrier frequency was adjusted to the best matching point for each setting of V_S. Inset: Capacitance sensitivity S_C as a function of V_M at optimal matching ($V_S = 6.8$ V, $f_C = 196$ MHz). The error bars derive from the height of the signal sideband compared to the scatter in the noise background.

IV. OPTIMIZING THE CAPACITANCE SENSITIVITY

We now show how to use the amplifier for sensitive measurements of capacitance. These measurements use a reflectometry configuration, in which the signal is injected via port 1 and the reflected signal is amplified by the SQUID. To avoid any contribution from the quantum capacitance, gate voltages are set to completely empty the quantum dot. To perform these measurements, we first tune the impedance of the tank circuit close to that of the measurement circuit and then characterize the sensitivity to changes in the capacitance.[18]

The capacitance sensitivity S_C is determined by modulating the varactor capacitance at a frequency f_M while driving the tank circuit at carrier frequency f_C. The reflected signal, monitored at port 2 using a spectrum analyzer, contains a main peak at f_C and sidebands at $f_C \pm f_M$. Such sidebands arise from mixing of an amplitude-modulated output signal when the impedance of the resonant circuit

is sensitive to the modulated quantity. S_C is extracted from the height of the sidebands above the noise floor (i.e., the signal-to-noise ratio or SNR, expressed in dB) according to[18,48,49]

$$S_C = \frac{\delta C}{\sqrt{2\Delta f}} 10^{-\mathrm{SNR}/20}, \tag{5}$$

where Δf is the spectrum resolution bandwidth and δC the root-mean-square modulation amplitude of the capacitance. To generate a capacitance modulation, we vary the control voltage of the varactor V_S with amplitude V_M, which is converted to the capacitance modulation δC as explained in the supplementary material.

A. Optimizing the matching circuit

To optimize the impedance matching between the tank circuit and the input network, we tune the varactor using V_S. Figure 5(a) shows the transmission $|S_{21}|$ from port 1 to port 2, which is proportional to the tank circuit's reflection coefficient, for different settings of V_S. The lowest reflection coefficient, and, therefore, the best match, is achieved at $f_C = 196\,\mathrm{MHz}$ when $V_S = 6.8\,\mathrm{V}$.

Figure 5(b) shows the capacitance sensitivity as a function of V_S measured with an input power of $P_1 = -60\,\mathrm{dBm}$ into port 1. This power corresponds to approximately $-154\,\mathrm{dBm}$ on the SQUID input and is well below the threshold of amplifier saturation. The best sensitivity is $S_C = 0.9 \pm 0.2\,\mathrm{aF}/\sqrt{\mathrm{Hz}}$. As expected, this occurs closest to perfect matching and, therefore, this varactor setting with the associated resonance frequency of 196 MHz is used in the remainder of Sec. IV.[18]

The inset of Fig. 5(b) is a plot of the sensitivity as a function of modulation amplitude V_M, measured using the optimized matching parameters. These data show that the sensitivity degrades at high modulation amplitude due to non-linearity of the varactor but confirm that the modulation applied in the main panel, $V_M = 99\,\mu\mathrm{V_{rms}}$, is within the linear range. In the following measurements (Sec. IV B), we choose an even smaller modulation amplitude of $V_M = 80\,\mu\mathrm{V_{rms}}$.

B. Optimizing the input power

Next, we study how the capacitance sensitivity depends on the carrier power P_1. Figure 6 shows that increasing P_1 improves the sensitivity, up to an optimal power of $P_1 = -31\,\mathrm{dBm}$, where the sensitivity reaches $S_C = 0.07 \pm 0.02\,\mathrm{aF}/\sqrt{\mathrm{Hz}}$. This power corresponds to approximately $-125\,\mathrm{dBm}$ incident on the amplifier input, given the known losses due to attenuation and reflection on the tank circuit following the signal path associated with input port 1. From $-31\,\mathrm{dBm}$ to around $-21\,\mathrm{dBm}$, the sensitivity stays roughly constant before worsening at higher input powers.

We interpret these three regimes using the flux-to-voltage transfer function of the SQUID $V_{OUT}(\Phi)$, as indicated by the insets in Fig. 6. For $P_1 < -31\,\mathrm{dBm}$, the amplifier is in its linear-response regime where the gain and the noise temperature are constant such that the sensitivity improves with increasing SNR at increasing input power. The region of approximately constant sensitivity between $-31\,\mathrm{dBm}$ and $-21\,\mathrm{dBm}$ indicates gain compression, which means that the flux $\delta\Phi$ induced by the input signal exceeds the linear range of $V_{OUT}(\Phi + \delta\Phi)$. This creates harmonics sidebands in the output spectrum such that the SNR around the main sidebands decreases. For $P_1 > -21\,\mathrm{dBm}$, when $\delta\Phi$ exceeds a quarter of a flux period, the amplifier reaches its saturation. At this point the flux oscillation reaches beyond the maxima and minima of $V_{OUT}(\Phi)$ and the sensitivity is degraded. The saturation threshold in Fig. 6 approximately matches the power threshold where T_N begins to worsen [Fig. 4(e)]. S_C does not follow the noise temperature exactly because increasing the carrier power affects both the signal and the noise. In the next paragraph, we will introduce a figure of merit that does not benefit from input power and follows the noise more closely.

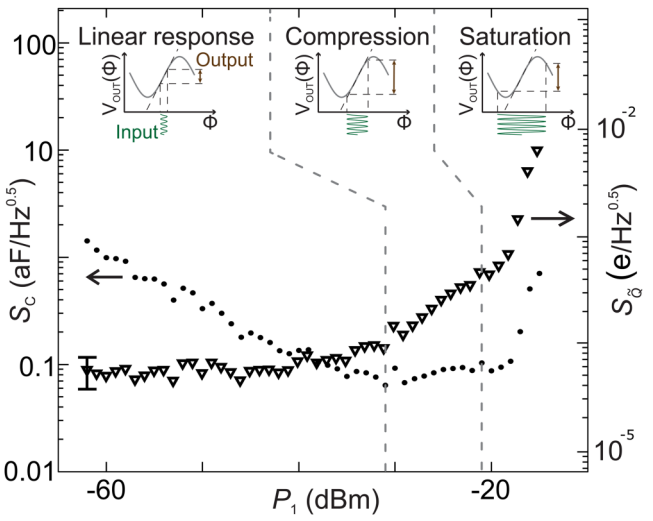

FIG. 6. Capacitance sensitivity S_C (left axis, points) and the sensitivity to a charge on one plate of the varactor $S_{\tilde{Q}}$ (right axis, triangles) as a function of the carrier power at port 1 P_1. The errors in S_C are smaller than the symbols and due to uncertainties in determining the noise level. The errors in $S_{\tilde{Q}}$ are due to uncertainties from the noise level as well as the input lines/cables. For clarity only one error bar is marked. Other parameters: $f_M = 3\,\mathrm{kHz}$, $V_M = 80\,\mu\mathrm{V_{rms}}$, $f_C = 196\,\mathrm{MHz}$ and $V_S = 6.8\,\mathrm{V}$. The insets illustrate the three operating regimes (see text) by marking the input and output signals on a graph of the flux-to-voltage transfer function $V_{OUT}(\Phi)$.

For dispersive readout of spin qubits, good capacitance sensitivity S_C is not sufficient to achieve high fidelity. One reason is that it may require a large RF bias, giving rise to back action by exciting unwanted transitions in the qubit device. Another reason is that the quantum capacitance is usually sizable only within a small bias range, so that increasing the RF excitation improves S_C without improving the qubit readout fidelity. This is the case for singlet–triplet qubits, where the quantum capacitance is large only near zero detuning.[11] As explained in the supplementary material, for dispersive readout the crucial sensitivity is to the oscillating charge induced on the gate electrode by the qubit capacitance, which in our setup corresponds to the charge induced on one plate of the varactor. This sensitivity is

$$S_{\tilde{Q}} = \sqrt{2} V_0 S_C, \tag{6}$$

where V_0 is the root-mean-square RF voltage across the device.[18] This is a key figure of merit for dispersive spin qubit readout. For single-shot readout, this sensitivity must allow for detecting a charge smaller than one electron within the qubit lifetime. We estimate V_0 using a circuit model of the tank circuit as in Ref. 18. For example, at $P_1 = -29$ dBm, the incident power onto the tank circuit is ~ 10 pW, giving an estimated voltage $V_0 = 192\,\mu V_{rms}$ across the device. The right axis of Fig. 6 shows $S_{\tilde{Q}}$ as a function of input power into port 1. $S_{\tilde{Q}}$ worsens at slightly lower input power than does S_C but reaches below $100\,\mu e/\sqrt{\text{Hz}}$ for optimal settings.

V. FAST READOUT OF A DOUBLE QUANTUM DOT

To demonstrate the full functionality of the circuit, we measure charge stability diagrams and determine the acquisition rate. We replace the single quantum dot from Fig. 1 with a double quantum dot operated in the Coulomb blockade regime.[50] For this experiment, we use a different SQUID amplifier which includes a feedback capacitor between V_{IN} and V_{OUT}, designed to lower its input impedance and thus improve the matching to the 50 Ω line impedance. We drive our circuit at $f_C = 210$ MHz with a power of $P_1 = -35$ dBm, which is just below the threshold for broadening the Coulomb peaks in the double dot. To form the double dot, we automatically adjust the gate voltages with the help of machine-learning algorithm.[31]

The charge stability diagram of the double dot is shown in Fig. 7(a), which plots the normalized signal amplitude $R = |V_I + iV_Q|$ as a function of the left and right plunger voltages V_L and V_R. This plot shows the characteristic honeycomb pattern of a double quantum dot. In the center of each honeycomb, the Coulomb blockade suppresses conductance, and the reflected signal is large [red regions in Fig. 7(a)]; at the honeycomb boundaries, the Coulomb blockade is partly lifted and the signal is small [blue regions in Fig. 7(a)].[29,51] As expected, the charge transitions of the left dot, closer to the RF electrode, give the strongest signal.

The low noise of the SQUID amplifier allows rapid measurement of the stability diagram. To show this, we focus on the region of the stability diagram marked by a dashed box in Fig. 7(a) and apply triangular waveforms via on-board bias tees to rapidly sweep V_L and V_R over this range. For these data, the filter time constant is set to $\tau = 1\,\mu$s. We record R during the upward ramps of the fast triangular waveform in order to build up a two-dimensional map [Fig. 7(b)]. The resolution is 100×100 data points, and the digitizer sample rate is 1 MHz, meaning that the entire plot is acquired within 20 ms. As expected, the resulting charge stability diagram, presented in Fig. 7(b), shows the same pattern as in Fig. 7(a), with easily distinguishable charge transitions despite the very short acquisition time.

The SNR can now be extracted directly by comparing a signal amplitude to the noise recorded in a time trace. The signal in this

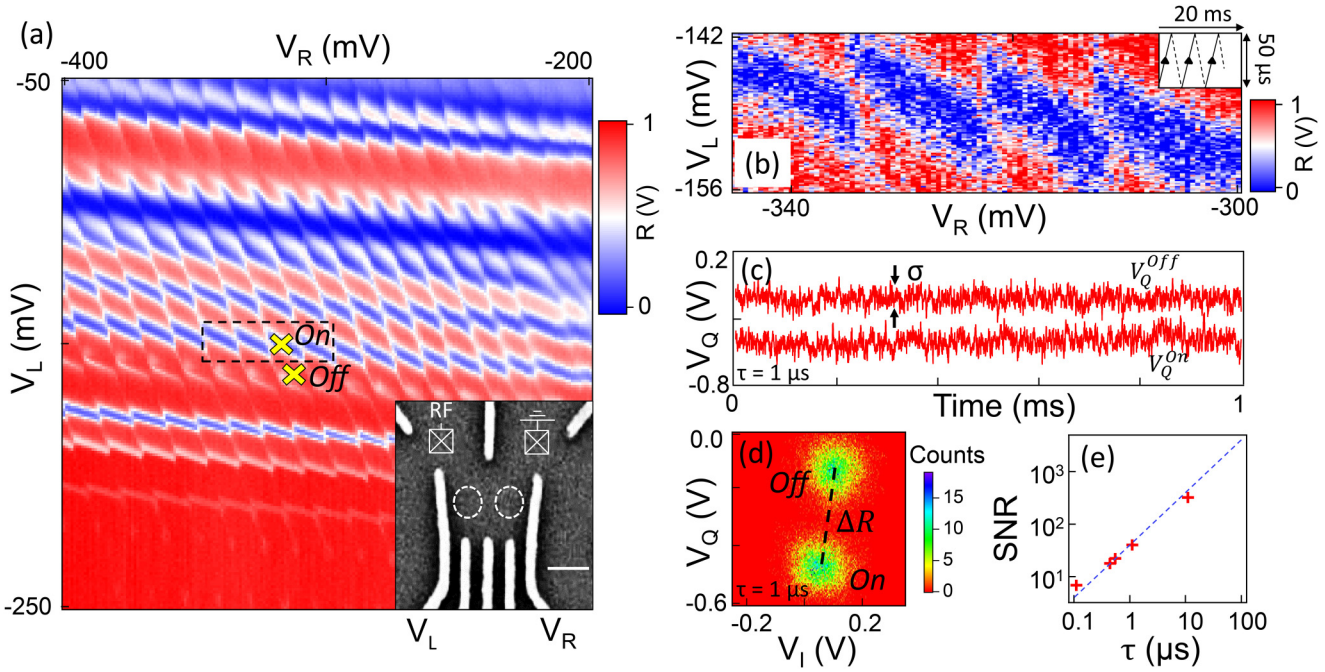

FIG. 7. (a) Reflected amplitude showing the double quantum dot charge stability diagram. The amplitude is normalized from 0 to 1 based on the minimum and maximum measured value. Inset: SEM image of the device. The scale bar is 200 nm long and the two dashed circles symbolize the two quantum dots. (b) Fast measurement of the charge stability diagram area highlighted by the dashed rectangular in (a) obtained with $\tau = 1\,\mu$s. V_L and V_R are swept using triangular waveforms as illustrated in the inset. (c) Time trace of normalized V_Q measured at the *On* and *Off* coordinates of (a), V_Q^{On} and V_Q^{Off}, respectively. σ is the standard deviation of the trace. (d) Joint histogram of recorded V_I and V_Q values for *On* and *Off*. (e) SNR as function of τ (symbols) and fit to Eq. (7) with $\tau_{min} = 25$ ns (line).

case is taken as the difference in reflected power between gate configurations on and off a Coulomb peak. To measure the SNR in Fig. 7(e), we record 10 000 samples of V_I and V_Q, digitized at a rate of 10 MHz, at two locations in the charge stability diagram in Fig. 7(a); V_I^{On} and V_Q^{On} at location marked by *On* and V_I^{Off} and V_Q^{Off} at location marked by *Off*. This experiment is repeated for different choices of filter time constant τ. A typical pair of time traces is shown in Fig. 7(c). Figure 7(d) represents these data as a joint histogram in the V_I vs V_Q quadrature space. The two well-separated Gaussian distributions show that the two Coulomb states can be distinguished within a single time interval of duration $\tau = 1\,\mu$s. The amplitude of the signal ΔR is defined as the distance between the mean values of the two distributions $\Delta R^2 = \left[\langle V_I^{On}\rangle - \langle V_I^{Off}\rangle\right]^2 + \left[\langle V_Q^{On}\rangle - \langle V_Q^{Off}\rangle\right]^2$ and the noise σ is their standard deviation (which as expected is the same in both V_I and V_Q channels). The signal-to-noise ratio $\mathrm{SNR} = \Delta R^2/\sigma^2$ is plotted as function of τ in Fig. 7(e). The blue dashed line is a fit according to

$$\mathrm{SNR} = \frac{\tau}{\tau_{\min}}, \tag{7}$$

with fit parameter $\tau_{\min} = 25$ ns, which is the extrapolated time to distinguish the two configurations with SNR of unity. The point at $\tau = 100$ ns falls slightly above the fit line because the integration time of the digital converter (100 ns) adds extra averaging. From these data, the sensitivity to a quasi-static charge of the double-dot device is at least as good as

$$S_{\Delta Q} \leq e\sqrt{\tau_{\min}} = 160\,\mu e/\sqrt{\mathrm{Hz}}. \tag{8}$$

In this expression, ΔQ is the difference in charge induced on the quantum dot between the two measured configurations, which is a large fraction of one electron charge.

In the supplementary material, we present a measurement of the sensitivity to a small charge modulation δQ, measured on the steep flank of a Coulomb peak using a single-dot device. This leads to a somewhat better sensitivity but is not directly comparable because it was measured using a different amplifier. Both these charge sensitivities are distinct from the sensitivity $S_{\tilde{Q}}$ plotted in Fig. 4; $\tilde{Q}$ is a charge oscillating in response to the RF field, whereas ΔQ and δQ are quasistatic charges. The former is what is measured in a dispersive measurement, the latter are what is measured using a charge sensor.

VI. DISCUSSION

We have shown that radiofrequency measurements, using a SQUID amplifier, can attain much better sensitivity than using a cryogenic semiconductor amplifier alone. This advantage holds when the signal level is limited by the need to avoid back-action on the device being measured, which is nearly always the case for quantum devices. The SQUID measured here has a gain around 12 dB and reaches a noise temperature below 600 mK, which is approximately seven times better than the (already optimized) semiconductor amplifier. When used to measure capacitance via radiofrequency reflectometry, it allows a record capacitance sensitivity of $S_C = 0.07 \pm 0.02\,\mathrm{aF}/\sqrt{\mathrm{Hz}}$, which corresponds to an improvement by a factor of 23 compared with the same setup without the SQUID.[18] This setup can also be used with a single quantum dot charge sensor. In the supplementary material, we perform this measurement and find a charge sensitivity of $S_{\delta Q} = 60 \pm 20\,\mu e/\sqrt{\mathrm{Hz}}$, corresponding to an improvement by a factor of 27 compared to the setup without the SQUID.[18] This improvement is better than expected from the improved noise temperature alone and probably also arises from lower cable loss and a different impedance matching condition to the amplifier input.

To put these results in the context of spin qubit readout, we estimate the dispersive readout time in a singlet–triplet qubit with the RF circuit connected to a plunger gate. In this case, a difference in capacitance on the order of 2 fF needs to be resolved to determine the state of the qubit.[11] Based on the capacitance sensitivity obtained in Sec. IV, we estimate a single-shot readout time of ~26 ns with our circuit (see supplementary material). Integrating a SQUID amplifier into a spin qubit setup should, therefore, significantly reduce the measurement noise, ultimately improving single-shot readout fidelity. This represents a major advantage for scalable quantum information processing architectures containing many qubits in a small space.[2,3]

As well as for qubit readout, this setup can also increase the sensitivity of other radiofrequency measurements. The fast measurements of a double quantum dot presented above demonstrate a minimum per-pixel integration time $\tau_{\min} \approx 25$ ns. This integration time is of the same order as the integration times in double-quantum dot measurements using Josephson parametric amplifiers[29,36] or high quality-factor microwave resonators[27] but was enabled by a commercially available amplifier without the need for a dedicated fabrication environment. In another application of our circuit, the improved sensitivity provided by the SQUID has enabled time-resolved measurements of a vibrating carbon nanotube transistor.[52]

SUPPLEMENTARY MATERIAL

See the supplementary material for more explanation of the charge sensitivity, charge sensing measurements on a single quantum dot, data from a separate cooldown of the amplifier, details of the measurement calibration, and full instructions for installing and tuning the amplifier.

AUTHORS' CONTRIBUTIONS

F.J.S. and F.V. contributed equally to this work.

ACKNOWLEDGMENTS

The work was funded by DSTL (Contract No. 1415Nat-PhD_59), EPSRC (Nos. EP/R029229/1 and EP/N014995/1), the Royal Academy of Engineering, a Marie Curie Fellowship, Templeton World Charity Foundation, the European Research Council (Grant Agreement No. 818751), and the Royal Society. Work in Basel was supported by the Swiss Nanoscience Institute (SNI), Swiss NSF (179024), and the EU H2020 European Microkelvin Platform EMP (824109). We thank M. Mück and ez SQUID for supplying and assisting with the amplifiers.

DATA AVAILABILITY

The data that support the findings of this study are available from the corresponding author upon reasonable request.

REFERENCES

[1]D. P. DiVincenzo and IBM, Fortsch. Phys. **48**, 771 (2000).
[2]M. Veldhorst, H. G. J. Eenink, C. H. Yang, and A. S. Dzurak, Nat. Commun. **8**, 1766 (2017).
[3]L. M. K. Vandersypen, H. Bluhm, J. S. Clarke, A. S. Dzurak, R. Ishihara, A. Morello, D. J. Reilly, L. R. Schreiber, and M. Veldhorst, npj Quantum Inf. **3**, 34 (2017).
[4]A. G. Fowler, M. Mariantoni, J. M. Martinis, and A. N. Cleland, Phys. Rev. A **86**, 032324 (2012).
[5]B. M. Terhal, Rev. Mod. Phys. **87**, 307 (2015).
[6]R. Hanson, L. P. Kouwenhoven, J. R. Petta, S. Tarucha, and L. M. K. Vandersypen, Rev. Mod. Phys. **79**, 1217 (2007).
[7]C. Barthel, D. J. Reilly, C. M. Marcus, M. P. Hanson, and A. C. Gossard, Phys. Rev. Lett. **103**, 160503 (2009).
[8]L. Gaudreau, G. Granger, A. Kam, G. C. Aers, S. A. Studenikin, P. Zawadzki, M. Pioro-Ladrière, Z. R. Wasilewski, and A. S. Sachrajda, Nat. Phys. **8**, 10 (2012).
[9]M. Veldhorst, C. H. Yang, J. C. C. Hwang, W. Huang, J. P. Dehollain, J. T. Muhonen, S. Simmons, A. Laucht, F. E. Hudson, K. M. Itoh, A. Morello, and A. S. Dzurak, Nature **526**, 410 (2015).
[10]J. R. Petta, A. C. Johnson, J. M. Taylor, E. A. Laird, A. Yacoby, M. D. Lukin, C. M. Marcus, M. P. Hanson, and A. C. Gossard, Science **309**, 2180 (2005).
[11]K. D. Petersson, C. G. Smith, D. Anderson, P. Atkinson, G. A. C. Jones, and D. A. Ritchie, Nano Lett. **10**, 2789 (2010).
[12]M. F. Gonzalez-Zalba, S. Barraud, A. J. Ferguson, and A. C. Betz, Nat. Commun. **6**, 6084 (2015).
[13]A. Crippa, R. Ezzouch, A. Aprá, A. Amisse, R. Laviéville, L. Hutin, B. Bertrand, M. Vinet, M. Urdampilleta, T. Meunier, M. Sanquer, X. Jehl, R. Maurand, and S. De Franceschi, Nat. Commun. **10**, 2776 (2019).
[14]A. Crippa, R. Maurand, D. Kotekar-Patil, A. Corna, H. Bohuslavskyi, A. O. Orlov, P. Fay, R. Laviéville, S. Barraud, and M. Vinet *et al.*, Nano Lett. **17**, 1001 (2017).
[15]C. Volk, A. Chatterjee, F. Ansaloni, C. M. Marcus, and F. Kuemmeth, Nano Lett. **122**, 5628 (2019).
[16]D. de Jong, J. van Veen, L. Binci, A. Singh, P. Krogstrup, L. P. Kouwenhoven, W. Pfaff, and J. D. Watson, Phys. Rev. Appl. **11**, 044061 (2019).
[17]M. Jung, M. D. Schroer, K. D. Petersson, and J. R. Petta, Appl. Phys. Lett. **100**, 253508 (2012).
[18]N. Ares, F. J. Schupp, A. Mavalankar, G. Rogers, J. Griffiths, G. A. C. Jones, I. Farrer, D. A. Ritchie, C. G. Smith, A. Cottet, G. A. D. Briggs, and E. A. Laird, Phys. Rev. Appl. **5**, 034011 (2016).
[19]J. I. Colless, A. C. Mahoney, J. M. Hornibrook, A. C. Doherty, H. Lu, A. C. Gossard, and D. J. Reilly, Phys. Rev. Lett. **110**, 046805 (2013).
[20]S. J. Hile, M. G. House, E. Peretz, J. Verduijn, D. Widmann, T. Kobayashi, S. Rogge, and M. Y. Simmons, Appl. Phys. Lett. **107**, 093504 (2015).
[21]A. C. Betz, R. Wacquez, M. Vinet, X. Jehl, A. L. Saraiva, M. Sanquer, A. J. Ferguson, and M. F. Gonzalez-Zalba, Nano Lett. **15**(7), 4622–4627 (2015).
[22]I. Ahmed, J. A. Haigh, S. Schaal, S. Barraud, Y. Zhu, C. M. Lee, M. Amado, J. W. A. Robinson, A. Rossi, J. J. L. Morton, and M. F. Gonzalez-Zalba, Phys. Rev. Appl. **10**, 014018 (2018).
[23]A. P. Higginbotham, T. W. Larsen, J. Yao, H. Yan, C. M. Lieber, C. M. Marcus, and F. Kuemmeth, Nano Lett. **14**, 3582 (2014).
[24]P. Pakkiam, A. V. Timofeev, M. G. House, M. R. Hogg, T. Kobayashi, M. Koch, S. Rogge, and M. Y. Simmons, Phys. Rev. X **8**, 041032 (2018).
[25]A. West, B. Hensen, A. Jouan, T. Tanttu, C.-H. Yang, A. Rossi, M. F. Gonzalez-Zalba, F. Hudson, A. Morello, and D. J. Reilly, Nat. Nanotechnol. **14**, 437 (2019).
[26]M. Urdampilleta, D. J. Niegemann, E. Chanrion, B. Jadot, C. Spence, P.-A. Mortemousque, L. Hutin, B. Bertrand, S. Barraud, R. Maurand, M. Sanquer, X. Jehl, S. De Franceschi, M. Vinet, and T. Meunier, Nat. Nanotechnol. **14**, 737 (2019).
[27]G. Zheng, N. Samkharadze, M. L. Noordam, N. Kalhor, D. Brousse, A. Sammak, G. Scappucci, and L. M. Vandersypen, Nat. Nanotechnol. **14**, 742 (2019).
[28]E. J. Connors, J. J. Nelson, and J. M. Nichol, Phys. Rev. Appl. **13**, 024019 (2020).
[29]J. Stehlik, Y. Y. Liu, C. M. Quintana, C. Eichler, T. R. Hartke, and J. R. Petta, Phys. Rev. Appl. **4**, 1 (2015).
[30]D. Lennon, H. Moon, L. C. Camenzind, L. Yu, D. M. Zumbühl, G. A. D. Briggs, M. A. Osborne, E. A. Laird, and N. Ares, npj Quantum Inf. **5**, 1 (2019).
[31]H. Moon, D. T. Lennon, J. Kirkpatrick, N. M. van Esbroeck, L. C. Camenzind, L. Yu, F. Vigneau, D. M. Zumbühl, G. A. D. Briggs, M. A. Osborne, D. Sejdinovic, E. A. Laird, and N. Ares, preprint arXiv:2001.02589 (2020).
[32]N. van Esbroeck, D. Lennon, H. Moon, V. Nguyen, F. Vigneau, L. C. Camenzind, L. Yu, D. M. Zumbühl, G. A. D. Briggs, D. Sejdinovic, and N. Ares, preprint arXiv:2001.04409 (2020).
[33]M. A. Castellanos-Beltran and K. W. Lehnert, Appl. Phys. Lett. **91**, 083509 (2007).
[34]T. Yamamoto, K. Inomata, M. Watanabe, K. Matsuba, T. Miyazaki, W. D. Oliver, Y. Nakamura, and J. S. Tsai, Appl. Phys. Lett. **93**, 042510 (2008).
[35]C. Macklin, K. O'Brien, D. Hover, M. E. Schwartz, V. Bolkhovsky, X. Zhang, W. D. Oliver, and I. Siddiqi, Science **350**, 307 (2015).
[36]S. Schaal, I. Ahmed, J. A. Haigh, L. Hutin, B. Bertrand, S. Barraud, M. Vinet, C.-M. Lee, N. Stelmashenko, J. W. A. Robinson, J. Y. Qiu, S. Hacohen-Gourgy, I. Siddiqi, M. F. Gonzalez-Zalba, and J. J. L. Morton, Phys. Rev. Lett. **124**, 067701 (2019).
[37]V. Vesterinen, O.-P. Saira, I. Räisänen, M. Möttönen, L. Grönberg, J. Pekola, and J. Hassel, Supercond. Sci. Technol. **30**, 085001 (2017).
[38]S. J. Chorley, J. Wabnig, Z. V. Penfold-Fitch, K. D. Petersson, J. Frake, C. G. Smith, and M. R. Buitelaar, Phys. Rev. Lett. **108**, 036802 (2012).
[39]A. C. Johnson, J. R. Petta, J. M. Taylor, A. Yacoby, M. D. Lukin, C. M. Marcus, M. P. Hanson, and A. C. Gossard, Nature **435**, 925 (2005).
[40]E. A. Laird, J. R. Petta, A. C. Johnson, C. M. Marcus, A. Yacoby, M. P. Hanson, and A. C. Gossard, Phys. Rev. Lett. **97**, 056801 (2006).
[41]M. Mück and R. McDermott, Supercond. Sci. Technol. **23**, 093001 (2010).
[42]A. Mavalankar, S. J. Chorley, J. Griffiths, G. A. C. Jones, I. Farrer, D. A. Ritchie, and C. G. Smith, Appl. Phys. Lett. **103**, 133116 (2013).
[43]A. Mavalankar, T. Pei, E. M. Gauger, J. H. Warner, G. A. D. Briggs, and E. A. Laird, Phys. Rev. B **93**, 235428 (2016).
[44]J. Clarke and A. I. Braginski, *The SQUID Handbook* (Wiley-VCH Verlag GmbH and Co. KGaA, Weinheim, 2005), pp. i–xvi.
[45]F. C. Wellstood, C. Urbina, and J. Clarke, Phys. Rev. B **49**, 5942 (1994).
[46]M. Mück, J. B. Kycia, and J. Clarke, Appl. Phys. Lett. **78**, 967 (2001).
[47]A. A. Clerk, M. H. Devoret, S. M. Girvin, F. Marquardt, and R. J. Schoelkopf, Rev. Mod. Phys. **82**, 1155 (2010).
[48]A. Aassime, G. Johansson, G. Wendin, R. J. Schoelkopf, and P. Delsing, Phys. Rev. Lett. **86**, 3376 (2001).
[49]H. Brenning, S. Kafanov, T. Duty, S. Kubatkin, and P. Delsing, J. Appl. Phys. **100**, 114321 (2006).
[50]L. C. Camenzind, L. Yu, P. Stano, J. D. Zimmerman, A. C. Gossard, D. Loss, and D. M. Zumbühl, Phys. Rev. Lett. **122**, 207701 (2019).
[51]W. G. Van der Wiel, S. De Franceschi, J. M. Elzerman, T. Fujisawa, S. Tarucha, and L. P. Kouwenhoven, Rev. Mod. Phys. **75**, 1 (2002).
[52]Y. Wen, N. Ares, F. J. Schupp, T. Pei, G. A. D. Briggs, and E. A. Laird, Nat. Phys. **16**, 75 (2019).

SUPPLEMENTARY MATERIAL

Sensitive radio-frequency read-out of quantum dots using an ultra-low-noise SQUID amplifier

F. J. Schupp[1,†], F. Vigneau[1,†], Y. Wen[1], A. Mavalankar[1], J. Griffiths[2], G. A. C. Jones[2], I. Farrer[2,3], D. A. Ritchie[2], C. G. Smith[2], L. C. Camenzind[4], L. Yu[4], D. M. Zumbühl[4], G. A. D. Briggs[1], N. Ares[1], and E. A. Laird[1,5*]

[1] *University of Oxford, Department of Materials, 16 Parks Road, Oxford OX1 3PH, UK*

[2] *Cavendish Laboratory, J.J. Thomson Avenue, Cambridge CB3 0HE, UK*

[3] *Department of Electronic and Electrical Engineering, University of Sheffield, Sheffield S1 3JD, UK*

[4] *Department of Physics, University of Basel, 4056 Basel, Switzerland*

[5] *Department of Physics, University of Lancaster, Lancaster, LA1 4YB, United Kingdom*

(Dated: May 21, 2020)

CONTENTS

S1. CHARGE SENSITIVITY AND QUBIT READOUT

Two distinct kinds of charge sensitivity are important in radio-frequency charge sensing, and both values are quantified in the main text. Here we clarify the difference between the two and explain how they are estimated.

A. Sensitivity to oscillating charge $S_{\tilde{Q}}$

Dispersive readout of a singlet-triplet qubit measures the effective quantum capacitance C_q that arises when an electron oscillates between two quantum dots [S1–S5]. The circuit is sensitive to the oscillating charge $\tilde{Q}$ on a nearby electrode. In order to distinguish singlet and triplet states, the sensitivity should be good enough to resolve the signal due to a single oscillating electron within the qubit relaxation time.

The sensitivity to oscillating charge $S_{\tilde{Q}}$ is related to the capacitance sensitivity S_C by

$$S_{\tilde{Q}} = \sqrt{2} V_0 S_C \tag{S1}$$

where V_0 is the root-mean-square RF voltage on the capacitor electrode. This follows from the fact that the amplitude of the charge oscillation on the electrode is $\tilde{Q} = \sqrt{2} V_0 C$. While Eq. (S1) suggests that the sensitivity could be improved without limit by increasing the injected RF voltage, this will not happen because the quantum capacitance of the singlet-triplet qubit exists only near zero voltage bias [S1]. To estimate the readout time, it is therefore necessary to average the quantum capacitance $C_\mathrm{q}(V)$ over an entire RF cycle [S5], i.e. to calculate

$$\overline{C_\mathrm{q}} = \frac{1}{2\sqrt{2}V_0} \int_{-\sqrt{2}V_0}^{\sqrt{2}V_0} C_\mathrm{q}(V) \mathrm{d}V \tag{S2}$$

where V is the instantaneous voltage on the gate electrode. The bandwidth for detecting this capacitance with unit SNR is then

$$\Delta f = (\overline{C_\mathrm{q}}/S_C)^2. \tag{S3}$$

In a double quantum dot, the quantum capacitance of the singlet state is:

$$C_\mathrm{q}(V) = (e\lambda)^2 \frac{(2t)^2}{2\left((\lambda e V)^2 + (2t)^2\right)^{3/2}} \tag{S4}$$

* e.a.laird@lancaster.ac.uk
† these authors contributed equally to this work

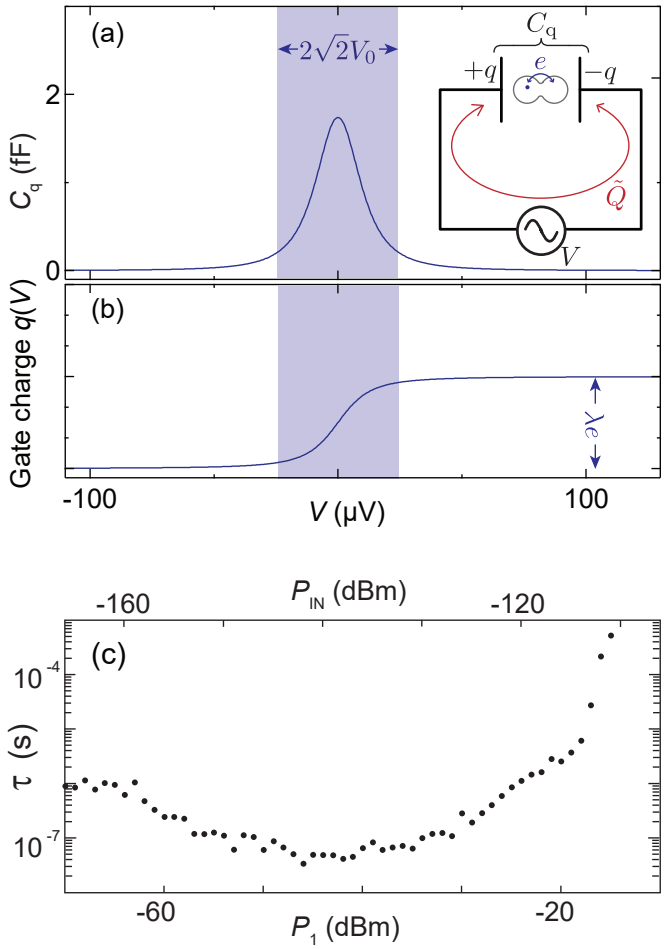

FIG. S1. Sensitivity to oscillating charge (a) Quantum capacitance of a double quantum dot as a function of voltage on the coupling electrode, from Eq. (S4). Inset cartoon: arrangement of drive voltage V, quantum capacitance C_q, instantaneous electrode charge q, and oscillating component of the electrode charge $\tilde{Q}$. (b) Charge on the coupling electrode, which acts as one plate of the capacitor. The shaded region is the range of an RF cycle over which the integral Eq. (S2) is calculated. (c) Read-out time $\tau = 1/2\Delta f$, estimated from Eq. (S3) and Fig. 4 of the main text. These data are plotted as a function of input power P_1 into port 1 (bottom axis) and of the corresponding power P_{IN} at the SQUID input (top axis).

where t is the inter-dot tunnel coupling and λ is the lever arm relating V to the detuning between the two dots. In a typical device [S1], $t = h \times 500$ MHz and $\lambda = 0.3$. This capacitance is plotted in Fig. S1(a), and the corresponding electrode charge $q(V)$ in Fig. S1(b).

To maximise the signal, the drive amplitude V_0 should be set larger than the peak width in Fig. S1(b). Equation (S2) then simplifies to

$$\overline{C_Q} = \frac{\lambda e}{2\sqrt{2}V_0} \tag{S5}$$

and the read-out bandwidth is:

$$\Delta f = \left(\frac{\lambda e}{2\sqrt{2}\,V_0 S_C}\right)^2 = \left(\frac{\lambda e}{2S_{\tilde{Q}}}\right)^2. \tag{S6}$$

To optimise the sensitivity, λ should be maximised while the product $V_0 S_C$ is minimised.

In this experiment, V_0 is limited not just by the width of the capacitance peak but also by the saturation threshold of the SQUID. Assuming the parameters from the device in Ref. [S1], the condition that the drive voltage exceeds the capacitance peak width, i.e. $V_0 \gtrsim t/\lambda e$, is reached around $P_1 = -31$ dBm in our setup. From the data in Fig. 2(e) of the main text we do not expect an increased SQUID amplifier noise until an input power of $P_{IN} = -120$ dBm (or P_1 around -27 dBm depending on the matching of the quantum dot device). The dynamic range of our setup is therefore sufficient for the device from Ref. [S1]. Devices with a larger lever arm $\lambda > 0.3$ are likely to require less input power to the SQUID amplifier, and therefore the dynamic range should not limit the circuit performance.

We can calculate the required read-out time for each value of V_0 (and thus P_1), by numerically integrating Eq. (S2) and substituting into Eq. (S3), using the values S_C measured in Fig. 4 of the main text. The read-out time is then given by $\tau = 1/2\Delta f$. The calculated values for the device from Ref. [S1], plotted in Fig. S1(c), reach an optimal value of $\tau = 26$ ns, implying that this singlet-triplet qubit could be read out in a single shot.

B. Sensitivity to quasi-static charge S_Q

In an electrometer configuration, the RF circuit detects a quasi-static charge Q via the resulting shift of a Coulomb peak. This is the configuration that is used when a charge sensing single-electron transistor (SET) is used for qubit readout [S6–S11]. In this configuration, the charge sensitivity, denoted S_Q, can be characterized in two ways. One way, used in Section V of the main paper, uses a gate voltage pulse to induce a large change ΔQ, on the order of one electron charge, to the equilibrium charge of the quantum dot device. As stated in the main paper, the estimated sensitivity in this case is

$$S_{\Delta Q} = e\sqrt{\tau_{\min}} \tag{S7}$$

where $\tau_{\min}$ is the measurement time that allows the change in device impedance to be resolved.

The other way to characterize the sensitivity is to modulate the gate voltage so as to induce a small charge δQ, and to measure the resulting sidebands that appear in the spectrum of the reflected signal. The sensitivity in this case is (analogous to Eq. 3 of the main text)

$$S_{\delta Q} = \frac{\delta Q}{\sqrt{2\Delta f}} 10^{-\mathrm{SNR}/20} \tag{S8}$$

where Δf is the measurement bandwidth and $\delta Q = e\,\delta V_L/\Delta V_{CB}$ is the induced charge variation on the quantum dot as a result of the gate modulation (in our measurement the left gate in Fig. 1 of the main text). Here ΔV_{CB} is the Coulomb peak spacing and δV_L is the gate modulation. In general $S_{\delta Q} \leq S_{\Delta Q}$.

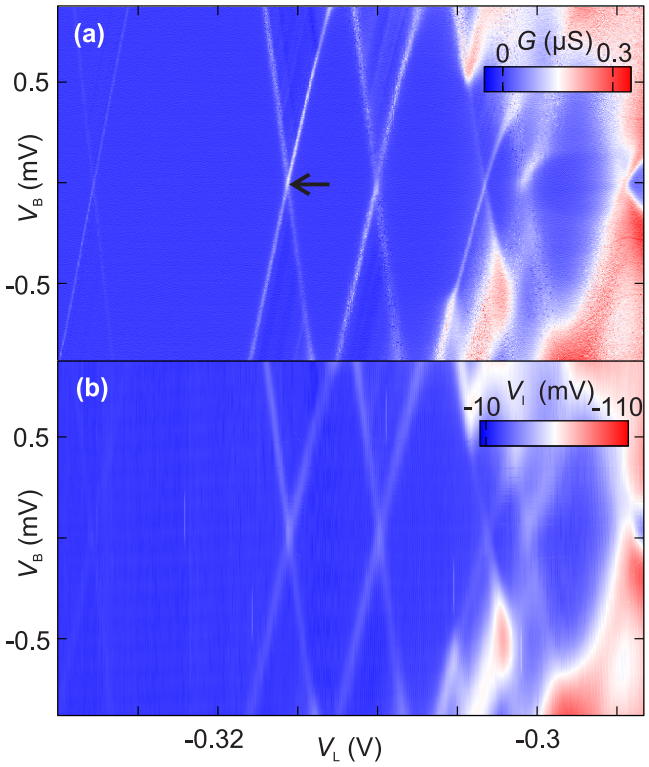

FIG. S2. Measurement of the single quantum dot device used in Section II-IV of the main text, in order to evaluate the sensitivity of a charge sensor. (a) Conductance G as a function of gate voltage V_L and bias voltage V_B. The black arrow indicates the Coulomb peak where the charge sensitivity was measured. (b) I quadrature, measured by homodyne detection (as in Fig. 1 of the main text) over the same range.

S2. CHARGE SENSING USING A SINGLE QUANTUM DOT

Here we measure again the single quantum dot device used in Section II-IV of the main text in order to operate this device as an electrometer for quasi-static charge.

A. Configuring the quantum dot as a single-electron transistor

To operate the quantum dot as an SET, we adjust the gate voltages to configure the quantum dot's tunnel barriers into the Coulomb blockade regime. We first measure the charge stability diagram at DC and at RF. Figure S2(a) shows the DC conductance G as a function of gate voltage V_L and source-drain bias voltage V_B while Fig. S2(b) shows the corresponding output voltage V_D of the RF detection circuit. Both measurements clearly show the Coulomb diamonds characteristic of single-electron transport [S12]. On the flank of a Coulomb peak, the dot's conductance and capacitance depend sharply on the electrochemical potential, making it a sensitive detector for electrical signals.

B. Measuring and optimising the charge sensitivity

To measure the charge sensitivity $S_{\delta Q}$, we center the gate voltage on the flank of a Coulomb peak ($V_L = -315.56$ mV, black arrow in Fig. S2(a)). Modulating the gate voltage while measuring the power spectrum of the reflected signal, we use Eq. (S8) to infer $S_{\delta Q}$.

The charge sensitivity is optimized in the same way as the capacitance sensitivity in the main text. In this section and in Figs. 2-6 we show how to optimize successively with respect to gate voltage V_L, varactor tuning voltage V_S, RF excitation P_1, and gate modulation amplitude δV_L. The aim is to operate on the flank of a Coulomb peak, where the change in sample impedance is maximized for a small gate voltage modulation. The ideal Coulomb peak is as sharp as possible in gate voltage and the peak conductivity is high. To find the most suitable Coulomb peak we begin the optimization by measuring the sensitivity $S_{\delta Q}$ as a function of gate voltage (Figure S3). As expected, the sensitivity is best on the flanks of the Coulomb peaks (compare Fig. 5 in the main text). The δQ used in Eq. (S8) is calculated taking account of the different Coulomb peak spacing in Fig. S3. The best sensitivity with these parameters is $S_{\delta Q} = 295\,\mu e/\sqrt{\text{Hz}}$ at a gate voltage of $V_L = -315.6$ mV (green marker in Fig. S3).

Next we optimize the sensitivity with respect to varactor voltage V_S (Fig. S4). In this measurement, we adjust the carrier frequency to the best matching point at each value of V_S. We find a sensitivity of $S_{\delta Q} = 182\,\mu e/\sqrt{\text{Hz}}$ at $V_S = 6.1$ V and $f_C = 194.56$ MHz (green marker in Fig. S4).

Figure S5 shows the optimization with respect to input power P_1 at port 1. As in Fig. 4 of the main text, the sensitivity improves with increasing signal, until it approaches the saturation threshold of the SQUID. The slightly different power dependence compared with Fig. 4 may result from the different impedance match condition. The best charge sensitivity $S_{\delta Q} = 93\,\mu e/\sqrt{\text{Hz}}$ is measured at $P_1 = -26$ dBm (green marker in Fig. S5).

Figure S6 shows the optimization of the sensitivity with respect to the amplitude δV_L. The sensitivity degrades slightly with increasing modulation amplitude because small non-linearities in the circuit (such as nonlinear device transconductance) scatter signal power into higher sidebands that are not measured. The best sensitivity in Figure S6 is $S_{\delta Q} = 80\,\mu e/\sqrt{\text{Hz}}$ measured at the lowest modulation amplitude $\delta V_L = 12\,\mu V_{\text{rms}}$. At even lower modulation amplitude, the signal becomes difficult to distinguish from external interference.

Finally we re-optimize the measurement with respect to gate voltage, holding other parameters at their optimal settings (Fig. S7). The final optimized sensitivity is $S_{\delta Q} = 60 \pm 20\,\mu e/\sqrt{\text{Hz}}$ at $V_L = -315.556$ mV. The associated power spectrum is shown in Fig. S8. This value of $S_{\delta Q}$ is about 27 times better than the previously achieved charge sensitivity in the same setup without the SQUID amplifier [S5].

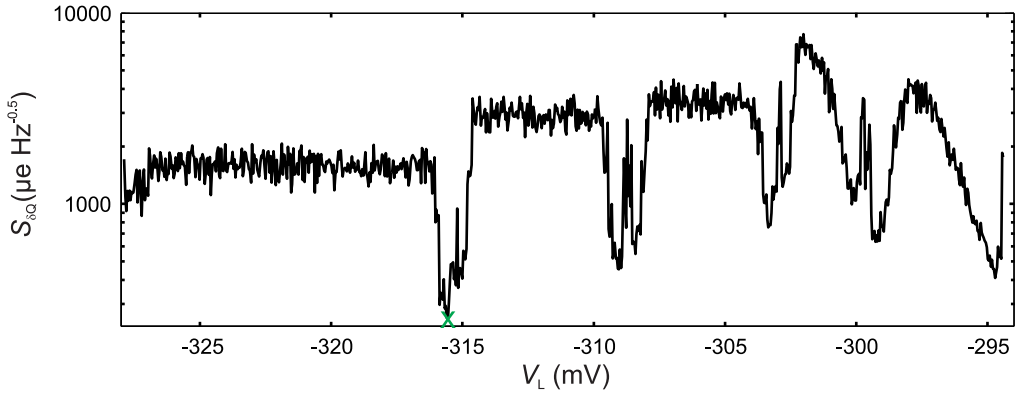

FIG. S3. Charge sensitivity $S_{\delta Q}$ as a function of gate voltage V_L at $f_C = 197\,\text{MHz}$, $V_S = 7\,\text{V}$, $f_M = 6\,\text{kHz}$, $\delta V_L = 117.8\,\mu\text{V}_{\text{rms}}$ and $P_1 = -38\,\text{dBm}$. The chosen gate voltage for further measurements $V_L = -315.6\,\text{mV}$ is indicated by the green marker.

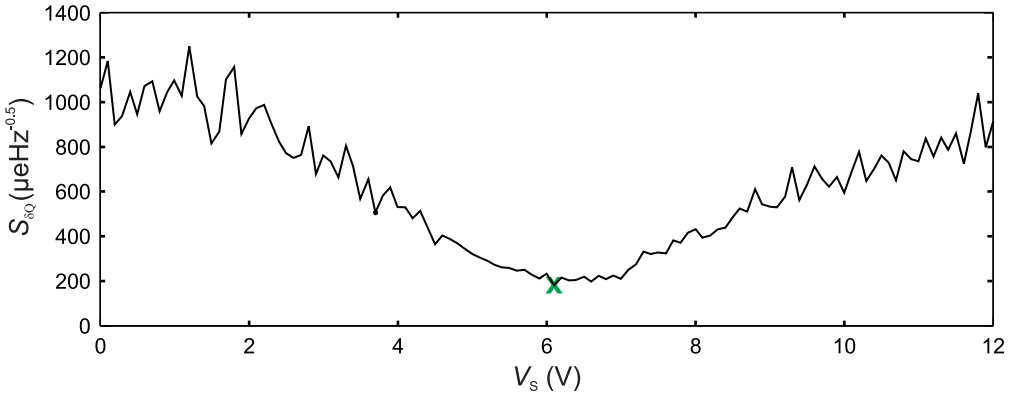

FIG. S4. Charge sensitivity $S_{\delta Q}$ as a function of varactor voltage V_S at $V_L = -315.6\,\text{mV}$, $f_M = 6\,\text{kHz}$, $\delta V_L = 117.8\,\mu\text{V}_{\text{rms}}$ and $P_1 = -38\,\text{dBm}$. The chosen varactor voltage for further measurements $V_S = 6.1\,\text{V}$ is indicated with the green marker. The associated carrier frequency is $f_C = 194.56\,\text{MHz}$.

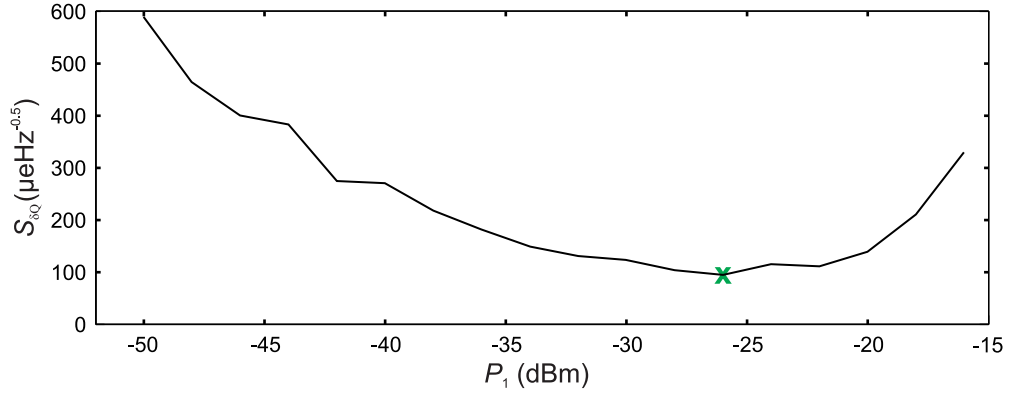

FIG. S5. Charge sensitivity $S_{\delta Q}$ as a function of power into port 1 P_1 at $V_L = -315.6\,\text{mV}$, $f_C = 194.56\,\text{MHz}$, $V_S = 6.1\,\text{V}$, $f_M = 6\,\text{kHz}$ and $\delta V_L = 117.8\,\mu\text{V}_{\text{rms}}$. The chosen $P_1 = -26\,\text{dBm}$ for further measurements is indicated by the green marker.

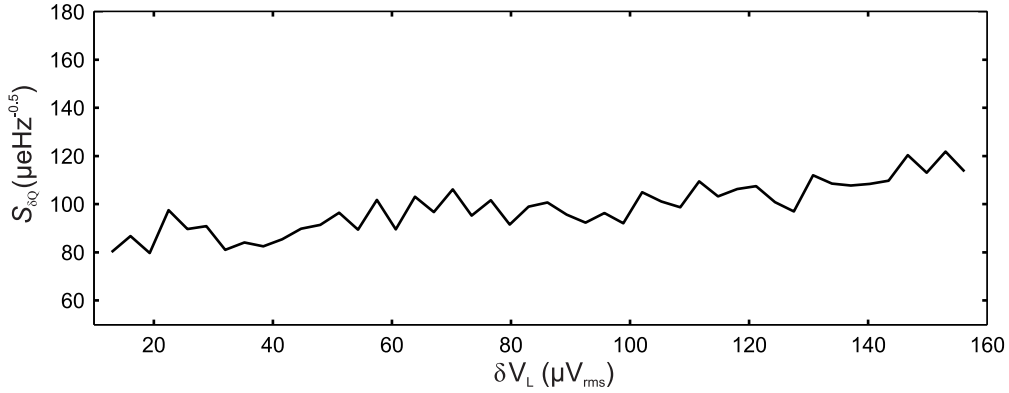

FIG. S6. Charge sensitivity $S_{\delta \mathrm{Q}}$ as a function of gate modulation amplitude δV_{L} at $V_{\mathrm{L}} = -315.6\,\mathrm{mV}$, $f_{\mathrm{C}} = 194.56\,\mathrm{MHz}$, $V_{\mathrm{S}} = 6.1\,\mathrm{V}$, $f_{\mathrm{M}} = 6\,\mathrm{kHz}$ and $P_1 = -26\,\mathrm{dBm}$. The best sensitivity is $S_{\delta \mathrm{Q}} \approx 80\,\mu e/\sqrt{\mathrm{Hz}}$.

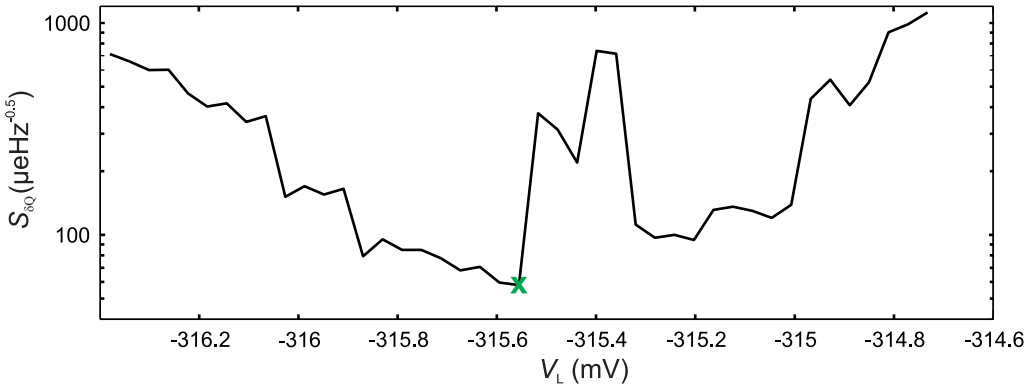

FIG. S7. Charge sensitivity $S_{\delta Q}$ as a function of gate voltage V_{L} at $\delta V_{\mathrm{L}} = 15.7\,\mu\mathrm{V_{rms}}$, $f_{\mathrm{C}} = 194.56\,\mathrm{MHz}$, $V_{\mathrm{S}} = 6.1\,\mathrm{V}$, $f_{\mathrm{M}} = 3\,\mathrm{kHz}$ and $P_1 = -26\,\mathrm{dBm}$. The best sensitivity, indicated with the green marker, is $S_{\delta Q} = 60 \pm 20\,\mu e/\sqrt{\mathrm{Hz}}$

.

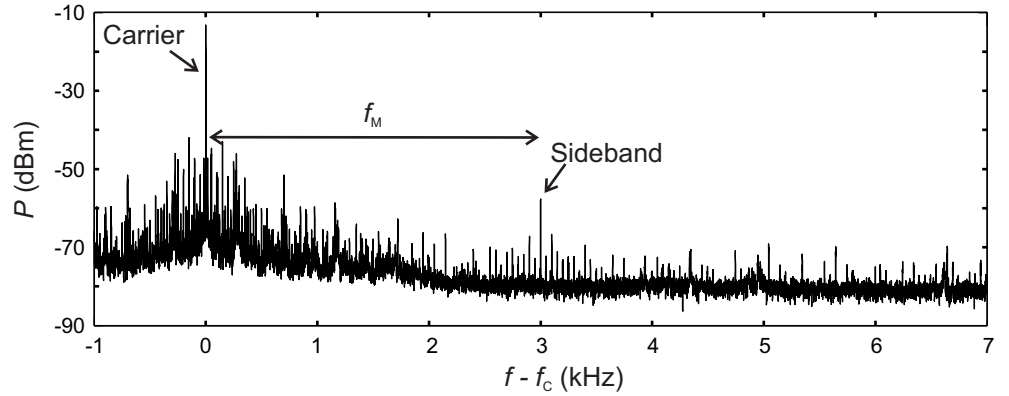

FIG. S8. Reflected power spectrum (after amplifier chain including room temperature amplifiers) in the sideband experiment for the best observed charge sensitivity in Fig. S7. The gate voltage setting is $V_{\mathrm{L}} = -315.556\,\mathrm{mV}$, as marked by the green cross in Fig. S7. The main spectral peak is the carrier tone, the marked peak is the modulation sideband, and the smaller peaks are residual interference signals.

For comparison, the best reported charge sensitivity in a semiconductor device, $S_{\delta Q} = 1.3\,\mu e/\sqrt{\text{Hz}}$ [S13], was measured using gate-based sensing, while the best reported value for reflectometry on the source contact is $S_{\delta Q} = 7.2\,\mu e/\sqrt{\text{Hz}}$ [S14]. Our charge sensitivity is therefore within one order of magnitude of the best reported values. Optimal charge sensitivity requires a small device resistance on the Coulomb peak [S15]. Whereas Ref. [S14] used a device with resistance on the Coulomb peak of 55 kΩ, the resistance in our device is 6.7 MΩ [S14, S15]. We therefore conclude that the charge sensitivity in our setup is limited by the device resistance and could be further improved with an optimized device, for which the tunnel barriers could be tuned to higher conductance while remaining within the Coulomb blockade regime.

S3. SQUID AMPLIFIER PERFORMANCE IN PREVIOUS COOLDOWN

Figure S9 shows the SQUID performance measured in a previous cooldown (before the cooldown in which the data from the main text was taken). In this measurement, the power was not yet optimized, which accounts for the elevated noise temperature of 800 mK, consistent with the power dependence in Fig. 2(e) of the main text. We also find that the optimal gain in Fig. S9(b) does not produce the lowest noise temperature in Fig. S9(d). This behaviour was previously linked to increased current noise close to the highest gain [S16].

Note that the critical current in this measurement is 12.9 µA at $I_\Phi = 0$. This is more than 2 µA higher than in Fig. 2(a) of the main text and presumably indicates a trapped flux. We have chosen $I_B = 13.1\,\mu A$ here and in the main text, in order to surpass the critical current regardless of flux.

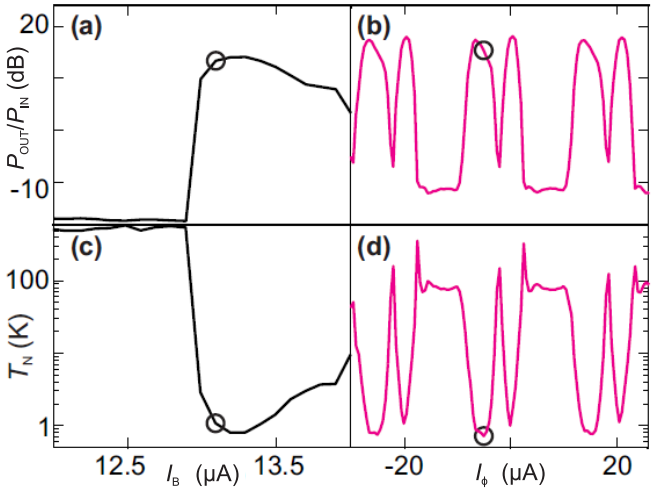

FIG. S9. SQUID amplifier performance in a previous cooldown and at a higher power $P_3 = -76$ dB.

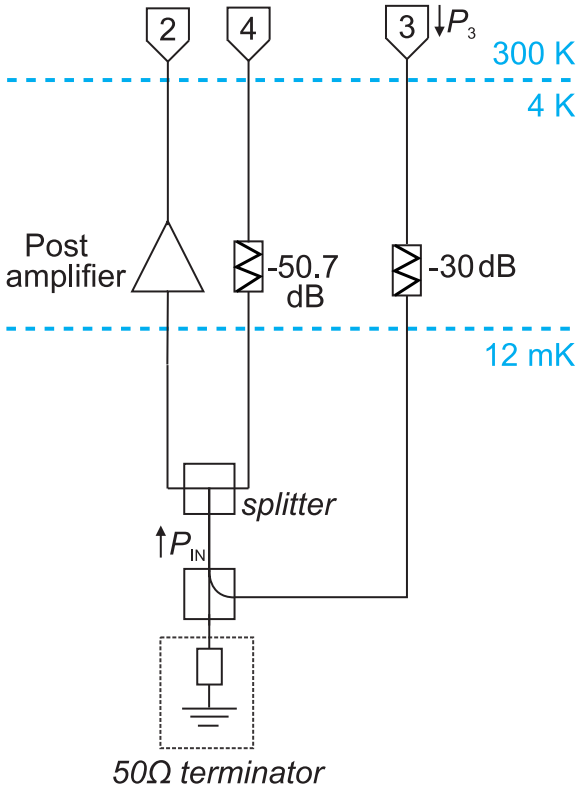

FIG. S10. Schematic of the line calibration measurement.

S4. DETAILS OF MEASUREMENT CALIBRATION

A. Determining the capacitance modulation δC

This section explains how to calculate the capacitance modulation δC, used in Eq. (3) of the main paper, from the known voltage modulation V_M across the varactor. From simulations and previous experiments [S5] with the same circuit and sample we know that the tank circuit behaves approximately as an LC resonator, whose resonance frequency is:

$$f_0(V_S) \approx \frac{1}{2\pi\sqrt{LC(V_S)}} \tag{S9}$$

where $L = 223$ nH is the inductor value and $C(V_S)$ is the capacitance as a function of varactor voltage. We can then infer the capacitance modulation δC from the voltage modulation V_M:

$$\delta C = \left|\frac{dC}{dV_S}\right| V_M = \frac{V_M}{2\pi^2 L f_0^3}\left|\frac{df_0}{dV_S}\right|. \tag{S10}$$

The measurements of Fig. 3 in the main text are used to extract the resonance frequency f_0 as a function of varactor voltage V_S and hence calculate $\frac{df_0}{dV_S}$ and δC.

B. Calibrating the input power to the amplifier chain

To measure the gain of the amplifier chain in our setup, we require a well-calibrated input power. The gain can then be determined by comparing the input and output power of the amplifier chain. Knowing this gain, together with the noise level at port 2, we can infer the noise level at the input of the SQUID amplifier.

To inject a known input power, we must know precisely the insertion loss of the input line from port 3. Although this insertion loss was confirmed at room temperature, we must further check it at low temperature to guard against small thermal variations in the cryogenic attenuators or other components. To do this, we introduce another line, entering the cryostat via port 4 (see Fig. S10), which allows the power entering the amplifier chain to be measured. The attenuation of the input line (i.e. via port 3) was now measured at base temperature in a dedicated cooldown, using the circuit shown in Fig. S10. In this measurement the tank circuit was replaced by a $50\,\Omega$ terminator on one side of the directional coupler. On the other side, the circuit was connected to a three-way symmetric resistive splitter that splits the signal equally into two lines: the RF measurement line (without the SQUID amplifier) and an additional line containing only attenuators. We know the low-temperature attenuation from the splitter to port 4, $|S_{4,\mathrm{sp}}|$, with a small error of $\pm 0.5\,\mathrm{dB}$, because this line was previously characterized in a simple transmission measurement in which it was driven through a nominally identical line. Assuming symmetry, the line attenuation is simply half the attenuation through the combined path. The symmetry of the resistive splitter was verified at room temperature.

We extract the gain in the RF measurement line $|S_{\mathrm{sp},2}|$ from the measurements of:

$$|S_{23}| = |S_{\mathrm{sp},3}| + \Delta + |S_{2,\mathrm{sp}}| \tag{S11}$$

and

$$|S_{43}| = |S_{\mathrm{sp},3}| + \Delta + |S_{4,\mathrm{sp}}| \tag{S12}$$

where Δ is the insertion loss of the splitter, and all quantities are expressed in dB. These two equations yield for the gain of the postamplifier line

$$|S_{2,\mathrm{sp}}| = |S_{23}| - |S_{43}| + |S_{4,\mathrm{sp}}| \tag{S13}$$

$$= 32 \pm 0.7\,\mathrm{dB} \tag{S14}$$

This value is in agreement with the specified gain of the postamplifier $34\pm2\,\mathrm{dB}$ taking account of a potential small loss in the rest of the measurement line.

We now extract $|S_{\mathrm{sp},3}|$, the insertion loss of the input line. To do this, we first infer the splitter loss by measuring the transmission S_{24}. Using the known attenuation $|S_{4,\mathrm{sp}}|$ and gain $|S_{2,\mathrm{sp}}|$, we extract $\Delta = |S_{24}| - |S_{\mathrm{sp},4}| - |S_{2,\mathrm{sp}}| = -6.1\,\mathrm{dB}$, close to the expected value for a three-way-symmetric resistive splitter. This value of Δ is then substituted into Eq. (S11) to infer an input insertion loss of $|S_{\mathrm{sp},3}| = 49.7\pm0.8\,\mathrm{dB}$, which agrees well with the expected losses from the inline attenuators (30 dB) and the directional coupler (20 dB). This is the value used when calculating the amplifier input power in the main text.

S5. INSTRUCTIONS FOR AMPLIFIER INSTALLATION AND TUNING

This section includes summary instructions from EZ-SQUID for installing and wiring the amplifier, a protocol for switching on the amplifier and a rough estimate of the expected dynamic range. By permission of EZ-SQUID, we have also provided their entire manual as Supplementary Material.

The original installation instructions from EZ-SQUID are:

As the bias resistors of the amplifier have only low resistance, you should add higher-value resistors at 4 K, say 100 kΩ for both currents. Connecting the amplifier directly to a room-temperature current source will couple too much noise to the SQUID. Also, if you want to measure gain, there must be at least 20 dB (30 dB would be better) of attenuation between the input of the amplifier and the room-temperature RF generator. It would also be good to decouple the output of the amplifier from the room-temperature network or spectrum analyzer by a post amplifier with sufficient gain. RF from the local oscillator of the network or spectrum analyzer coupled back into the output of the amplifier might saturate the SQUID otherwise. Finally, wireless LAN can also saturate the amplifier if the bias leads will pick up RF.

In the setup from the main text, the DC lines are filtered using an array of RC filters at the mixing chamber (total inline resistance 5.36 kΩ, total capacitance 330 pF, with Minicircuits LFCNxx RF filters and a printed circuit board meander embedded in copper powder). The RF input lines have at least 30 dB of attenuation and the output line is connected to the postamplifier sitting at 4 K. For thermalization, we wrap the amplifier in copper braid around the SMA connectors under the shield and clamp the copper braid to the mixing-chamber plate. In the future, the thermalization could be improved with a dedicated holder and shielding.

After installation and cooldown, we recommend the protocol following Sec. III of the main text:

1. Sweep current bias while monitoring the transmission through the amplifier. The critical part in this step is choosing an input power that produces signal above the noise level of the measurement when the amplifier transmission increases above the critical current. At the same time, the input power should not saturate the amplifier. As a rule of thumb, the maximum input power can be estimated by using half of the critical current as the maximum output swing. For a critical current of 10 μA and

a SQUID impedance of 15 Ω, this corresponds to a power at the output around −64 dBm. A good guess for an input power would then depend on the expected amplification. For the amplifiers in the main text with a gain around 12 dB (which might be underestimated due to reflections on the amplifier input), we should then easily be in the linear regime with a power on the input below −100 dBm. It is advisable, however, to choose the lowest possible power as the exact gain and the extent of other saturating effects (such as thermal excitations) are unknown.

2. Fix the bias current above the critical current, where you should see increased transmission in the sweep from step 1. Since the critical current depends on the flux bias, it is advisable to leave a few μA margin between the critical current and the chosen bias current to account for trapped flux. Once the bias current is fixed, sweep the flux bias current optimizing the gain in the transmission measurement. If the gain is not a smooth function as a function of flux bias around the highest gain, the bias current might be too small or the input power too high, such that you have reached the compression regime. Another reason could be noise in the bias current or flux.

3. Choose a flux bias associated with optimized performance and characterize the amplifier as needed for the experiment. This can include a measurement of the dynamic range as in Fig. 3(e) of the main text or a frequency sweep. Note that the input impedance, and therefore the dynamic range, depends on frequency.

[S1] K. D. Petersson, C. G. Smith, D. Anderson, P. Atkinson, G. A. C. Jones, and D. A. Ritchie, Nano Letters **10**, 2789 (2010).

[S2] J. Colless, A. Mahoney, J. Hornibrook, A. Doherty, H. Lu, A. Gossard, and D. Reilly, Physical Review Letters **110**, 046805 (2013).

[S3] J. Verduijn, M. Vinet, and S. Rogge, Applied Physics Letters **104**, 102107 (2014).

[S4] M. F. Gonzalez-Zalba, S. Barraud, A. J. Ferguson, and A. C. Betz, Nature Communications **2**, 1 (2015).

[S5] N. Ares, F. J. Schupp, A. Mavalankar, G. Rogers, J. Griffiths, G. A. C. Jones, I. Farrer, D. A. Ritchie, C. G. Smith, A. Cottet, G. A. D. Briggs, and E. A. Laird, Physical Review Applied **5**, 034011 (2016).

[S6] R. J. Schoelkopf, Science **280**, 1238 (1998).

[S7] J. M. Elzerman, R. Hanson, J. S. Greidanus, L. H. Willems van Beveren, S. De Franceschi, L. M. K. Vandersypen, S. Tarucha, and L. P. Kouwenhoven, Physical Review B **67**, 161308 (2003).

[S8] J. R. Petta, A. C. Johnson, J. M. Taylor, E. A. Laird, A. Yacoby, M. D. Lukin, C. M. Marcus, M. P. Hanson, and A. C. Gossard, Science **309**, 2180 (2005).

[S9] D. J. Reilly, C. M. Marcus, M. P. Hanson, and A. C. Gossard, Applied Physics Letters **91**, 162101 (2007).

[S10] M. C. Cassidy, A. S. Dzurak, R. G. Clark, K. D. Petersson, I. Farrer, D. A. Ritchie, and C. G. Smith, Applied Physics Letters **91**, 6 (2007).

[S11] C. Barthel, D. J. Reilly, C. M. Marcus, M. P. Hanson, and A. C. Gossard, Physical Review Letters **103**, 160503 (2009).

[S12] R. Hanson, L. P. Kouwenhoven, J. R. Petta, S. Tarucha, and L. M. K. Vandersypen, Reviews of Modern Physics **79**, 1217 (2007).

[S13] I. Ahmed, J. A. Haigh, S. Schaal, S. Barraud, Y. Zhu, C.-m. Lee, M. Amado, J. W. A. Robinson, A. Rossi, J. J. L. Morton, and M. F. Gonzalez-Zalba, Physical Review Applied **10**, 014018 (2018).

[S14] S. J. Angus, A. J. Ferguson, A. S. Dzurak, and R. G. Clark, Applied Physics Letters **92**, 112103 (2008).

[S15] A. N. Korotkov and M. A. Paalanen, Applied Physics Letters **4052**, 3 (1999).

[S16] B. Schmidt and M. Mück, Applied Physics Letters **100**, 152601 (2012).

SQUID Radio Frequency Amplifiers

The SQUID is the most sensitive detector of magnetic flux available. SQUIDs have long been used for a wide-range of low-frequency applications, including gravity wave detection, susceptometry, biomagnetism, nondestructive evaluation, and magnetic resonance imaging. There has been recent interest in the development of low-noise radio frequency and microwave amplifiers for particle detection, the readout of infrared sensors, or measurement of superconducting quantum bits. For these applications the SQUID has emerged as a leading candidate, as due to its extremely low power dissipation and unsurpassed noise properties.

In a typical SQUID amplifier, the input signal is converted to a current, which is injected into a thin-film input coil that is tightly coupled to the SQUID washer. The input current induces a flux in the SQUID, which in turn generates an output voltage V_o, which is a function of the applied flux (see Fig.1a). As the flux threading the SQUID loop changes, the voltage across the current-biased SQUID changes with periodicity Φ_0 (Fig. 1b).

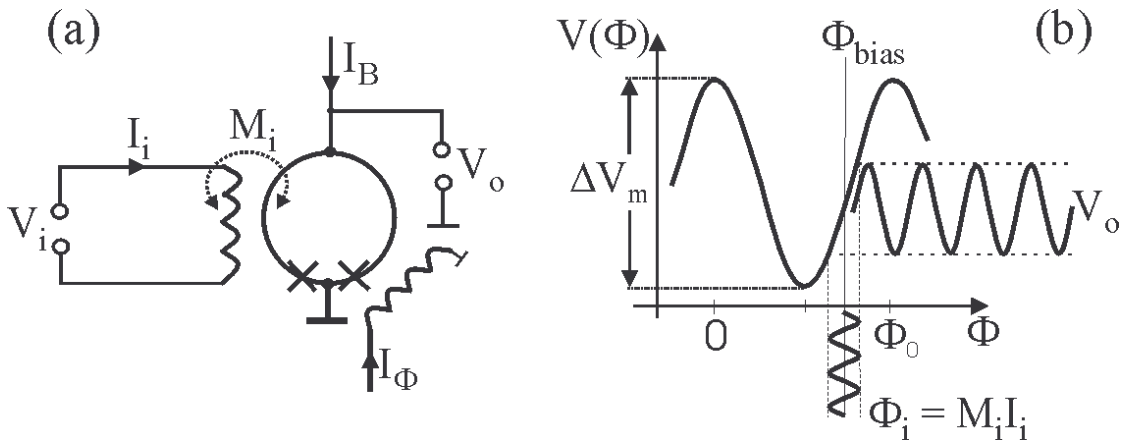

Fig. 1. (a). Configuration of dc SQUID amplifier. (b) Voltage vs flux for a current-biased dc SQUID showing conversion of an input flux Φi to an output voltage *Vo*.

To maximize the output voltage V_o, a static flux of $(2n-1)\Phi_0/4$ must be added to the ac input signal so as to bias the device at the steepest point of the $V(\Phi)$ curve. This is usually accomplished by passing a dc current I_Φ through a small wire-wound coil tightly coupled to the SQUID and adjusting this dc current for maximum gain.

The Microstrip SQUID Amplifier

To obtain maximum gain in a SQUID amplifier, the coupling between the input coil and the SQUID should be ~1. This can be achieved by integrating the input coil directly on top of the SQUID in thin-film technology. However, as an integrated input coil in a

washer-type SQUID is separated from the SQUID washer only by a thin insulating film, coil and washer thus form a capacitor in parallel to the input coil inductance. Because of this parasitic capacitance, the input circuit is purely inductive only at frequencies below the self-resonant frequency of the tuned circuit formed by the coil and the parasitic capacitance. Above this resonant frequency, the gain drops quickly.

The deleterious effect of the parasitic capacitance of the input circuit can be addressed by operating the input coil of the SQUID as a transmission line resonator in the so-called microstrip SQUID amplifier (MSA). In this approach, one makes a virtue of the capacitance between the coil and the washer by using it to form a resonant microstrip, see Fig. 2 (b).

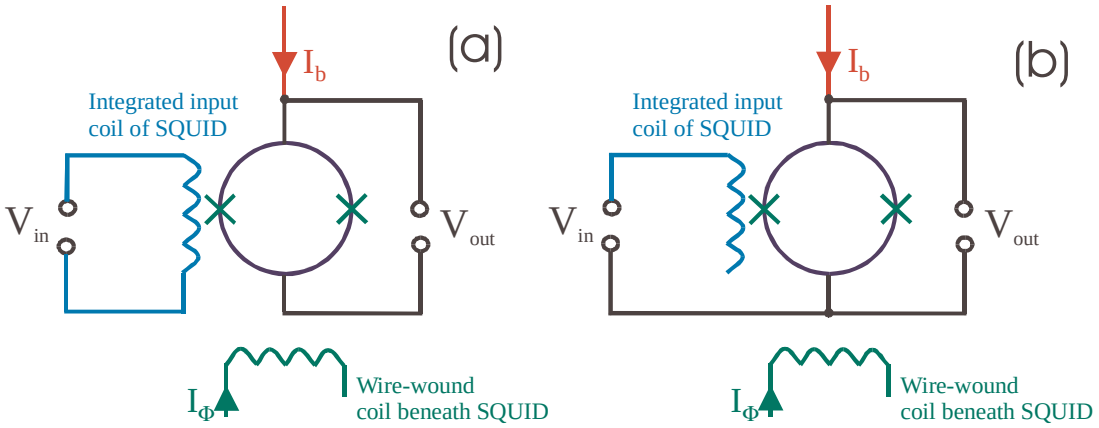

Fig.2 (a) Conventional SQUID amplifier; the input signal is coupled to both ends of the input coil. (b) Microstrip SQUID amplifier; the input signal is coupled to one end of the coil and the SQUID washer; the other end of the coil is left open.

The signal to be amplified is applied between one end of the coil and the washer, while the other end of the coil is left open (Fig. 2 (b)). Provided that the source impedance is greater than the characteristic impedance of the microstrip, there is a peak in the gain when the input coil accommodates approximately (but not exactly) one half wavelength of the input signal. Gains of well over 20 dB and noise temperatures well below the bath temperature can be achieved. We note that the actual behavior of the device differs markedly from that of a simple microstrip with a continuous ground plane because the inductance coupled into the input coil from the SQUID is generally substantially greater than the intrinsic microstrip inductance.

Operation of a microstrip SQUID amplifier

The SQUID amplifier requires two adjustable dc bias currents. One is passed in the SQUID to bias the it just above its critical current (SQUID bias, ~ 10 - 20 μA), the other

one (flux bias) is produced by a coil close to the SQUID to flux bias the SQUID at a steep point on its V-Φ curve.

To adjust the bias currents for highest gain, one applies a signal to the SQUID amplifier (say, -100 dbm) and observes the output of the SQUID on a spectrum analyzer. Even if the SQUID does not amplify, there will be a small amount of rf passing through the SQUID. If possible, increase the rf level so that rf can be seen at the output of the SQUID. The SQUID bias current is now slowly increased. As the bias current exceeds the critical current of the SQUID (~ 10 - 20 μA, depending on the SQUID), the output signal of the amplifier increases (or at least changes). If the input power to the amplifier is above, say, -100 dBm, decrease it to a level at which the signal can still be observed, but is substantially lower than -100 dBm. Then adjust the flux bias for maximum gain. Due to internal feedback, the gain at a bias flux of $\Phi_0/4$ will be different from that at a bias flux of $3\Phi_0/4$.

Note that the input signal to the SQUID amplifier must always be below -100 dBm or so, as, otherwise, the amplifier might saturate. In this case, the gain will drop and the noise temperature will increase.

There is only one optimum setting for the SQUID current bias. The optimum flux bias setting is periodic in Φ_0. As external magnetic fields will also change the flux bias of the SQUID, the gain might drift or be modulated with changing external fields. If an ac-magnetic interference were present, the gain of the amplifier would be modulated by the interference. The amplifier is packaged in a stainless-steel tube. Thus, a superconducting magnetic shield must be used. The simple shield supplied consists of a lead-foil cylinder with an outer layer of (ferromagnetic) Conetic AA foil.

The bias currents to the SQUID and the wire-wound coil producing the static flux bias are applied through enameled copper wires inside a teflon sleeve, which are connected to a four-pin connector (2.54-mm pin separation, as used, e.g. in sockets for integrated circuits). Another wire (thick yellowish) is used for ground connection (not really required as the ground is also connected to the stainless-steel tube of the amplifier and the SMAs). A fourth wire is connected to a 1-kΩ resistor to ground, which can be used as a heater. The thicker wire with the yellowish enamel is ground. The wire with the green enamel is the bias current for the SQUID, the red wire is the current to the coil producing the static field. The purple wire is connected to the heater. The SQUID is very sensitive to electrostatic discharge. DO NOT touch the metallic parts of the connector ! Never solder to the connector !

There is a dc block between the SQUID output and the output SMA connector. The SMA input connector is directly coupled to the microstrip resonator on the SQUID, which is electrically insulated from the SQUID by a 400 nm-thick SiO film. Thus, there will be no dc current flowing in the input and output of the amplifier. However,

especially at the input, any dc potential should be very small (~ mV) to prevent damage to the microstrip resonator. Also, the SQUID could be damaged by static discharge if the inner pin of the SMA connectors were touched.

There is a slight possibility that the Josephson junctions of the SQUID trap flux during cool down. As the critical current of the SQUID is reduced then, the gain might be relatively small or even zero. In this case the amplifier should be warmed up to above 9 K to remove the trapped flux. This can be done by passing a current in the 1-kΩ resistor used as a heater. This will only work if the amplifier is in a vacuum. If the amplifier is immersed in liquid helium, simply raise the amplifier to above the helium level to shortly warm it to T > 9 K. It should not be necessary to use the heater if there are no large fields present during cool down, and so the purple wire for the heater can be left unconnected.

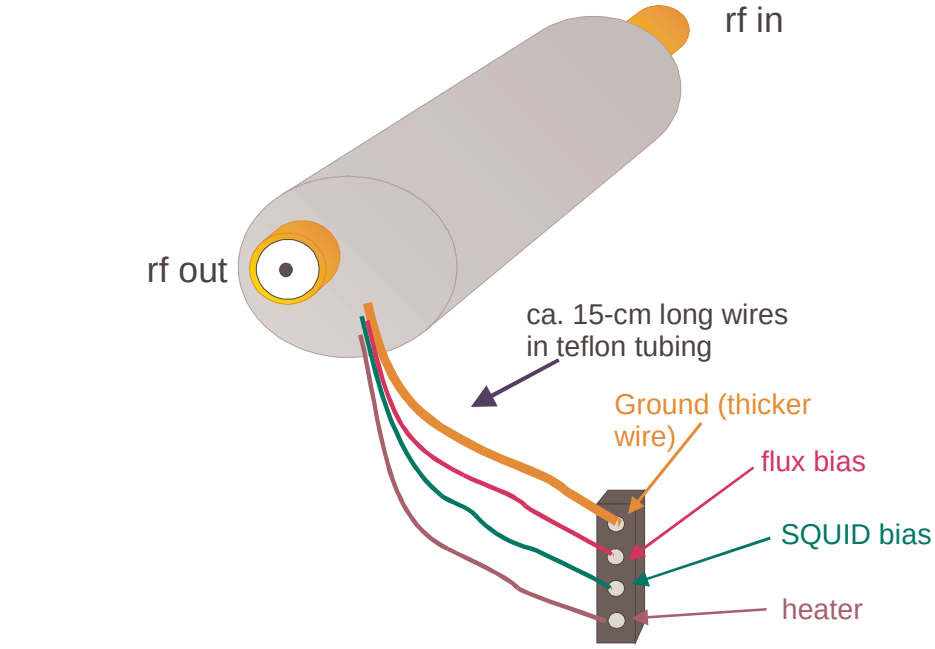

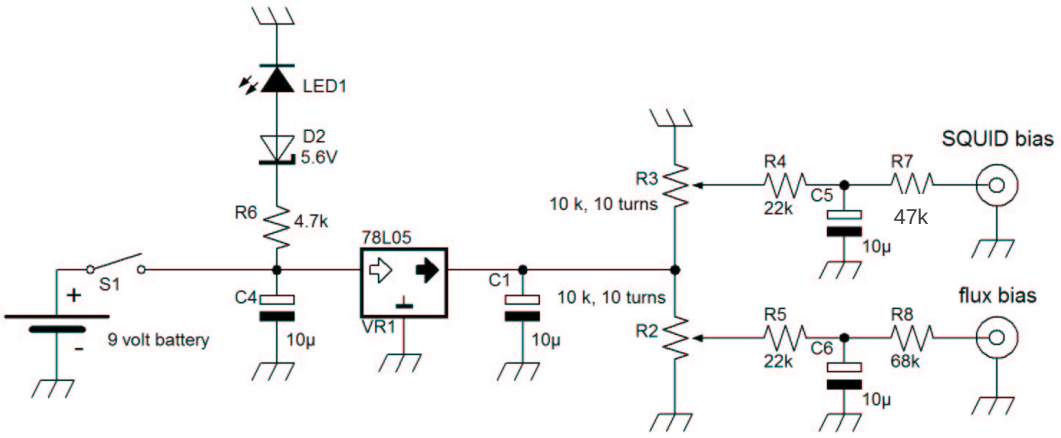

Suggestion for a SQUID-amplifier power supply.